The Functional Nasal Anatomy of the Pike, *Esox lucius* L.

Russell J. Garwood[a], Julia Behnsen[b], Andrew T. Ramsey[c], Harriet K. Haysom[d], Luke J. Dalby[e], Samuel K. Quilter[e], James S. Maclaine[f], Zhijin Wang[g], Jonathan P. L. Cox[d]

[a]*Department of Earth and Environmental Sciences, University of Manchester, Manchester, M13 9PL, UK*

[b]*Henry Moseley X-ray Imaging Facility, University of Manchester, Manchester, M13 9PY, UK*

[c]*Nikon Metrology, 12701 Grand River Avenue, Brighton, MI 48116, USA*

[d]*Department of Chemistry, University of Bath, Bath, BA2 7AY, UK*

[e]*TotalSim, Top Station Road, Brackley, NN13 7UG, UK*

[f]*Department of Life Sciences, Natural History Museum, Cromwell Road, London, SW7 5BD, UK*

[g]*Department of Mechanical Engineering, University of Bath, Bath, BA2 7AY, UK*

MS has 55 pages, 17 figures, 1 video, 1 appendix

Declaration of interest: None

*Corresponding author
Dr Jonathan P.L. Cox
Department of Chemistry
University of Bath
Bath, BA2 7AY, UK
Tel. +44 1225 386548
j.p.l.cox@bath.ac.uk

Abstract

Olfactory flow in fishes is a little-explored area of fundamental and applied importance. We investigated olfactory flow in the pike, *Esox lucius*, because it has an apparently simple and rigid nasal region. We characterised olfactory flow by dye visualisation and computational fluid dynamics, using models derived from X-ray micro-computed tomography scans of two preserved specimens. An external current induced a flow of water through the nasal chamber at physiologically relevant Reynolds numbers (200 – 300). We attribute this externally-induced flow to: the location of the incurrent nostril in a region of high static pressure; the nasal bridge deflecting external flow into the nasal chamber; an excurrent nostril normal to external flow; and viscous entrainment. A vortex in the incurrent nostril may be instrumental in viscous entrainment. Flow was dispersed over the olfactory sensory surface when it impacted on the floor of the nasal chamber. Dispersal may be assisted by: the radial array of nasal folds; a complementary interaction between a posterior nasal fold and the ventral surface of the nasal bridge; and the incurrent vortex. The boundary layer could delay considerably (up to ~ 3 s) odorant transport from the external environment to the nasal region. The drag incurred by olfactory flow was almost the same as the drag incurred by models in which the nasal region had been replaced by a smooth surface. The boundary layer does not detach from the nasal region. We conclude that the nasal bridge and the incurrent vortex are pivotal to olfaction in the pike.

Keywords: Artificial chemical sensor; 3D printing; pressure coefficient; streamline; sturgeon.

1. Introduction

The anatomy of a fish determines how water flows in and around its nasal region (Theisen, 1982). Olfactory flow in turn determines how odorants are transported to the olfactory epithelium (Zeiske et al., 1992; Cox, 2008). Effective odorant transport requires flow through the fish's nasal chamber (Cox, 2008), and dispersal of flow over the olfactory epithelium (Holmes et al., 2011). But odorant transport must contend with the presence of a boundary layer on the surface of the fish (Denny, 1993, p. 138-140; Cox, 2008). Furthermore, olfactory flow will incur drag, and so exact a metabolic cost.

Here we report the functional nasal anatomy of the pike, *Esox lucius* (Esocidae; Nelson, 2006, p. 205). We chose the pike, a predatory fish that occupies a wide range of habitats (Craig, 2008), for the following reasons. First, its nasal anatomy appears simple (Fig. 1C – F; Burne, 1909; Holl, 1965). Second, its nasal anatomy suggests that flow of water through the nasal chamber may be induced by an external flow (Burne, 1909; Cox, 2008), i.e. by the fish moving forward, and/or by an environmental water current. Raat (1988, p. 52) in fact states that water flows through the nasal chamber only when the pike moves, although there is no evidence for this claim in the reference he cites (Devitsina and Malyukina, 1977). Third, the nasal region appears rigid, and so may be faithfully represented by a rigid plastic model. Finally, there are no moving macroscopic parts in the nasal region to complicate olfactory flow.

We investigated the functional nasal anatomy of the pike by addressing the following questions. 1) Can flow through the nasal chamber be induced by an external flow? 2) If so, how? 3) How is flow dispersed over the olfactory epithelium? 4) How does the boundary layer influence odorant transport? 5) What drag does the nasal region incur? Boundary layers and drag have been mentioned before in relation to olfactory flow in fishes (Cox, 2008; Agbesi et al., 2016a, 2016b), but not quantified.

We tackled these questions using the complementary techniques of dye visualisation and computational fluid dynamics (Garwood et al., 2019). The anatomically-accurate models employed in our experiments were derived from X-ray micro-computed tomography scans of two well-preserved specimens whose nasal anatomy differs in several important age-related respects. We compare the results from the models of both specimens. We also compare olfactory flow in the pike with that in the sturgeon. We do so because the sturgeon's nasal

region is like that of the pike (Cox, 2008), and because flow through the nasal chamber of the sturgeon is externally-induced (Garwood et al., 2019). Readers unfamiliar with fluid dynamics are referred to Shapiro (1961) and Vogel (1994).

2. Materials and methods

Most of the methodology used here has been described before (Cox, 2008; Abel et al., 2010; Holmes et al., 2011; Howard et al., 2013; Ramsey et al., 2015; Garwood et al., 2019). We therefore give only brief descriptions here. Further details are given in the Appendix. Values for the density and dynamic viscosity of water are taken from Haynes and Lide (2011, p. 6-7), and Table 1 of Goldstein (1965), respectively.

2.1. Preserved specimens

The two preserved specimens of the pike, *Esox lucius* (Fig. 1), used to construct the models are from the Natural History Museum, London, UK. The first specimen (catalogue number BMNH 1963.4.26.2), which we refer to as the juvenile pike, was caught by dip net on 19 August 1962 at the mouth of the Kandik River, Alaska, USA. The second specimen (catalogue number BMNH 1986.5.20.4), which we refer to as the adult pike, was caught (method of capture not recorded) on 7 May 1986 in the Mill Stream, East Stoke, Dorset, UK. The fork lengths (Fig. 1A, *FL*; Fig. 2.2 of Helfman et al., 2009) and wet weights of the specimens are 18.5 cm and 40 g (juvenile pike), and 34 cm and 380 g (adult pike). The fork lengths of the specimens indicate that they were about one year old (juvenile pike) and two years old (adult pike) when caught (Table 4.1 of Craig, 1996). Since capture, both specimens have been stored in 70 % industrial methylated spirits, 30 % distilled water.

2.2. In vivo *observations*

Four pike (*FL* ~ 75 – 100 cm) were observed *in vivo* at the Aquarium of the Lakes, Cumbria, UK, 4 – 5 June 2015. We refer to these specimens as the aquarium specimens. The nasal anatomy of 11 additional specimens (*FL* = 10 – 50 cm) was observed *in vivo* (but with the specimens temporarily out of water) during a joint Environment Agency/University of Bournemouth (both UK) survey at Tewkesbury and Upton Marinas, River Severn, UK, on 22 June 2017. (We did not participate in this survey.) The 11 specimens, which we refer to as the survey specimens, were captured by seine net and, following observation, returned to the water alive. Regulated procedures completed on the survey specimens were performed by Environment Agency/University of Bournemouth personnel under UK Home Office licence 70/8063 and after ethical review.

2.3. X-ray micro-computed tomography

X-ray micro-computed tomography (micro-CT) of the preserved specimens was done at Nikon Metrology, Tring, UK (juvenile pike) and at the Henry Moseley X-ray Imaging Facility, University of Manchester, UK (adult pike) using an XT H 225 system. Both scans were performed in air. The scan of the juvenile pike comprised 1807 TIFF images (e.g. Fig. 2A) and had a voxel size of 29 μm x 29 μm x 29 μm ([dataset] Ramsey et al., 2019). The scan of the adult pike comprised 1772 TIFF images (e.g. Fig. 2B) and had a voxel size of 52 μm x 52 μm x 52 μm ([dataset] Garwood et al., 2020). Both scans extended from the rostral tip to the gill region (Fig. 1C and D). Further details of the scans are given in Appendix A.1.1.

2.4. Surface models

Surface models of the heads of the juvenile and adult pike were generated with the image processing software ScanIP (Synopsys, Mountain View, USA) as previously described (Garwood et al., 2019). We prepared two types of surface model: 'wild type' models (Fig. 3; [dataset] Haysom et al., 2020), in which the nasal regions of the model were intact, and 'mutant' models (Fig. A.7, Appendix A.5; [datasets] Haysom et al., 2020), in which the nostrils and nasal chamber of each nasal region were replaced by a continuous surface that blended smoothly with the rest of the head. The mutant models were used in the CFD simulations, specifically for the drag calculations, and to investigate the boundary layer in the nasal region (Section 2.7). Unless otherwise stated, any reference to a surface model is to the wild type model. Further details of the surface models are given in Appendix A.1.2 and A.1.7.4.

2.5. Plastic models

The plastic models of the heads (both wild type; Fig. 4) were either 3x (juvenile pike) or 2x (adult pike) life size. The plastic models were larger than life to allow us to see clearly dye behaviour in the nasal region (Section 2.6). Fabrication and assembly of the models are described in Appendix A.1.3.

151

152 *2.6. Dye visualisation*

153 Dye visualisation was performed in an Eidetics Model 1520 closed-circuit, free-surface,
154 continuous-flow flume (Wang et al., 2007) using the plastic models of the juvenile and adult
155 pike heads. To obtain a well-defined dye filament, we operated the flume at a free-stream
156 speed of 5 cm s^{-1}. This speed corresponded to Reynolds numbers of 200 – 300 for both
157 models (Section 2.9.2), a range indicative of laminar flow (Vogel, 1994, pp. 84-85).
158 According to the principle of dynamic similarity (Shapiro, 1961, p. 74; Vogel, 1994, p. 102),
159 a speed of 5 cm s^{-1} with the 3x life-sized model of the juvenile pike corresponds to a free-
160 stream speed of 15 cm s^{-1} for the actual specimen, or 0.8 *FL* s^{-1} (*FL* = 18.5 cm; Section 2.1).
161 Similarly, a speed of 5 cm s^{-1} with a 2x life-sized model of the adult pike corresponds to a
162 free-stream speed of 10 cm s^{-1} for the actual specimen, or 0.3 *FL* s^{-1} (*FL* = 34 cm; Section
163 2.1). These free-stream speeds fall into the range of environmental currents (≤ 30 cm s^{-1}) and
164 swimming speeds (0.08 – 4 *FL* s^{-1}) a stationary/cruising pike may encounter/adopt (Appendix
165 A.1.4 and A.1.5; Webb, 1984). We therefore consider Reynolds numbers of 200 – 300 to be
166 physiologically relevant.

167

168 The pitch and yaw (Fig. 10.1 of Barnard and Philpott, 2004) of the plastic models were both
169 0°. Roll angles (ibid.) are specified in the legends for the video clips. Flow was visualised
170 with red food dye diluted in a ratio of four parts water to one part dye. The water temperature
171 in the flume varied between 12 – 16.5 °C, and changed by ≤ 2.5 °C in a single day. Dye
172 visualisation experiments were recorded on a Panasonic HC-V500 digital camcorder (50
173 frames s^{-1}, 1920 pixels x 1080 pixels per frame) mounted on a Velbon DV-7000 tripod fitted
174 with a Vel-flo 9 PH-368 head. Footage was analysed using the software Adobe Premiere Pro
175 CC. Further details of the dye visualisation experiments are given in Appendix A.1.6.

176

177 *2.7. Computational fluid dynamics*

178

179 *2.7.1. General*

180 Computational fluid dynamics (CFD) simulations of olfactory flow in the pike were
181 performed on life-sized models of both the juvenile and the adult pike. The simulations were
182 run using the software OpenFOAM (Weller et al., 1998). The surface of each CFD mesh was
183 refined in the nasal region (Fig. 5A). Adjacent to the surface of the nasal region, the mesh

comprised five layers of cells (Fig. 5C, inset). The thickness of these cells was sufficient to capture the velocity gradients here. The number of cells across the nasal passage was 40 – 50 (e.g. Fig. 5C). Simulations were run at inlet velocities of 15 cm s^{-1} (juvenile pike) and 10 cm s^{-1} (adult pike), corresponding to Reynolds numbers of 200 – 300 (Section 2.9.3), and therefore matching the Reynolds numbers for the dye visualisation experiments (Section 2.6). Pitch and roll were 0°; yaw was 0 ± 5° (positive and negative yaw angles are indicated in Fig. 3A). Simulations in which yaw was varied were only performed for the wild type models. For a particular simulation, the density and dynamic viscosity were set to either: 999.2 kg m^{-3} and 1.2 x 10^{-3} Pa s; or 999.1 kg m^{-3} and 1.1 x 10^{-3} Pa s (values for water at 14 and 15 °C, respectively). Flow was assumed to be steady, laminar (Section 2.6), isothermal, and incompressible. The assumption of steady flow was based on initial transient simulations. In the transient simulation for the juvenile pike, the static pressure in the centre of both types of nostril (incurrent and excurrent) was found over 4 s to vary by < 0.03 % of the average static pressure at these locations over that time period (Fig. A.6, double-asterisked line, Appendix A.5). In the transient simulation for the adult pike, the flow rate through a plane of refined cells in each nostril (e.g. Fig. 5C of Garwood et al., 2019) was found over 12 s to vary by < 0.02 %. Velocities, static pressures, and shear stresses were the averages of the last 500 iterations from a total of 2000 iterations of a converged, time-averaged solution to the Navier-Stokes equations. Convergence was checked by monitoring the volumetric flow rate through a plane of refined cells in each nostril of both the juvenile and the adult pike. Because the volumetric flow rate through these planes changed by ≤ 0.03 % over the last 500 iterations of the simulations, we assumed convergence had occurred. Results from the CFD simulations were analysed and visualised with ParaView (Ayachit, 2016). Full details are given in Appendix A.1.7. Because flow was steady in the CFD simulations, the streamlines generated in ParaView equate to pathlines (Kline, 1972), and therefore indicate the path a fluid particle takes (Barnard, 2009, p. 6). Further details of the simulations are given in Appendix A.1.7.1.

2.7.2. Pressure

Static pressures are expressed as pressure coefficients (*Cp*; Douglas et al., 1985; Vogel, 1988), i.e. the ratio of the static pressure (P-P_0) to the dynamic pressure of the free-stream flow ($\frac{1}{2}\rho U_0^2$):

$$C_p = \frac{P - P_0}{\frac{1}{2}\rho U_0^2}$$

Equation 1

where P is the static pressure at a given point, P_0 is the ambient static pressure of the fluid (set to zero in the CFD simulations), ρ is the density of the fluid (999.1 or 999.2 kg m^{-3}; above), and U_0 is the free-stream speed (inlet velocity = 10 or 15 cm s^{-1}).

The fraction of the dynamic pressure of the free-stream flow harnessed by the nasal region (ΔC_p) was calculated using Equation 2:

$$\Delta C_p = C_p \text{ (Incurrent nostril)} - C_p \text{ (Excurrent nostril)} \qquad \text{Equation 2}$$

where C_p (Incurrent nostril) and C_p (Excurrent nostril) are the average pressure coefficients for the fluid in the incurrent and excurrent nostrils, respectively. ΔCp is given as a percentage in the ensuing text.

Details of how we located points of static pressure on the surface of a CFD model and of how we calculated the static pressure in each nostril are given in Appendix A.1.7.2.

2.7.3. Boundary layer

We gauged the thickness of the boundary layer on the surfaces of the model pike using vorticity (Abernathy, 1972; Thwaites, 1960, p. 18). (We did not use speed to gauge the boundary layer thickness because the contours of speed were not asymptotic in the nasal region; Fig. A.9C and D, Appendix A.5). We defined the thickness of the boundary layer using a vorticity of 5 s^{-1}. This value gave a contour within ParaView that was a) smooth and b) located in a similar position to the dorsal limit of the dye filament in the dye visualisation experiments involving the adult pike model (Section 3.2). Values less than 5 s^{-1} gave noisier contours. Details of how we estimated the thickness of the boundary layer are given in Appendix A.1.7.5, together with details of how we estimated the time taken for a fluid particle to get from the point of entry into the boundary layer to the incurrent nostril.

2.7.4. Drag

Drag was estimated using the method described in Appendix A.1.7.6. The drag-related figures given in Table 1 are for the two *combined* nasal regions.

2.8. Morphometry

Morphometric measurements (e.g. nasal chamber volumes) were made using ParaView, Rhinoceros (Version 4.0, Robert McNeel & Associates), and ScanIP, according to previous methodology (e.g. Garwood et al., 2019, Appendix A.1.5). Morphometric measurements were made on both the left and right nasal regions.

2.9. Reynolds numbers

2.9.1. General

Reynolds numbers (*Re*) for olfactory flow were calculated using either Equation 3 (Vogel, 1994, p. 85) or Equation 4 (Holmes et al., 2011):

$$Re = \frac{UL\rho}{\mu}$$

Equation 3

$$Re = \frac{4Q\rho}{L\mu}$$

Equation 4

where U is the speed of the fluid, L is the characteristic dimension of the object, μ is the dynamic viscosity of the fluid, and Q is the volumetric flow rate. For external olfactory flow, U was the free-stream speed (U_0), and L was the width of the nasal region in dorsal profile, normal to the direction of flow (Fig. 6B). For internal olfactory flow, L was the wetted perimeter of the nasal chamber (Fig. 2A and B, yellow lines). Reynolds numbers are given to one significant figure.

2.9.2. Reynolds numbers for dye visualisation

The Reynolds numbers for olfactory flow in the dye visualisation experiments were calculated (Equation 3) with U = 5 cm s^{-1} (the free-stream speed in the flume; Section 2.6), L

= 6 mm (juvenile pike) or 7 mm (adult pike), ρ = 998.9 – 999.5 kg m^{-3}, and μ = 1.1 – 1.2 x 10^{-3} Pa s at 12 – 16.5 °C (water temperature in the flume; Section 2.6).

2.9.3. Reynolds numbers for CFD

Calculations of Reynolds numbers for olfactory flow in the CFD simulations used the values of speed (inlet velocity), density, and dynamic viscosity given in Section 2.7.1. Reynolds numbers for olfactory flow were calculated (Equation 3) with L = 1.9 mm (juvenile pike) or 3.4 mm (adult pike). Reynolds numbers for flow through each nasal chamber were calculated (Equation 4) with Q = 10 mm^3 s^{-1} (juvenile pike) or 60 mm^3 s^{-1} (adult pike), and L = 6 mm (juvenile pike) or 12 mm (adult pike). Volumetric flow rates were determined according to Appendix A.1.6 of Garwood et al. (2019). The slices used to determine each flow rate are shown in Fig. 5C, and Fig. A.5C, Appendix A.5.

2.10. Videos and figures

In keeping with our work on the sturgeon (Garwood et al., 2019), the video clips (see Video, Supplementary data) and figures are shown in the same orientation, with the anterior part of the head or nasal region to the left. In dorsal views, the lateral part of the head is always uppermost. Unless stated otherwise, the video clips and figures show the *right* side of the specimens or models. Superior views are those normal to the nasal region. Copyright of the images of the specimens belongs to the Natural History Museum, London, UK.

3. Results

3.1. Nasal anatomy

The nasal anatomy of the two specimens from which we created our models is consistent with previous descriptions of the pike's nasal anatomy (Burne, 1909; Teichmann, 1954; Holl, 1965), and with our observations of pike *in vivo* (Section 2.2). Each of the two nasal regions (Fig. 7) comprises a nasal chamber (Fig. 8, yellow outlines) linked to the external environment by an incurrent nostril and an excurrent nostril (Figs. 7 and 8, IN and EN). The volumes of the nasal chambers were 3 and 20 mm^3 (juvenile and adult pike, respectively). The ratio of the area of the incurrent nostril to that of the excurrent nostril was 1:1 in both specimens. The incurrent nostril is separated from the excurrent nostril by a nasal bridge (Figs. 7 and 8, NB). The dorsal edge of the nasal bridge protrudes from the surface of the head (Fig. 8, asterisked sections). Internally, the incurrent nostril is connected to the excurrent nostril by a single (nasal) passage (Figs. 8 and 9, NP). A radial array of low folds occupies the floor of the nasal chamber (Fig. 10). We refer to this array as the olfactory rosette, and to the folds as nasal folds (Figs. 8 and 10, NF). The sensory olfactory epithelium resides in patches between the nasal folds, but not on the folds themselves (Fig. 1F, inset, white regions; Figs. 26 and 27 of Holl, 1965). Consequently, we refer to the channels formed by adjacent nasal folds as sensory channels (Figs. 7, 9 and 10, green disks). Finally, there is a complementary interaction between the central posterior nasal fold (Fig. 9, yellow disks) and the ventral surface of the nasal bridge (Fig. 9, asterisks).

3.2. Dye visualisation

Using dye visualisation, we established that flow of water through the nasal chambers of the model pike could be induced by free-stream flow at Reynolds numbers of 200 – 300 (Fig. 11A – F; Video clips 1 – 10). In doing so, we observed that:

1) The rostrum deflected dye into the nasal region (Fig. 11B; Video clips 2 and 3). 2) Dye fanned in front of the nasal region (Video clips 4 and 7). Such behaviour indicated that flow was decelerating and therefore that the nasal region was a region of relatively high static pressure (Shapiro, 1972). 3) Dye entered the nasal chamber via the incurrent nostril, and exited via the excurrent nostril, confirming the roles of these two apertures (Fig. 11A – F). 4) Within the nasal chamber, dye took either a medial or a lateral route (Fig. 11D, Me and Lt;

Videos clips 6 and 7). 5) Dye could circulate in the incurrent nostril in a manner suggestive of a vortex (Fig. 11E, blue disk; Video clips 8 and 9; Lugt, 1983). 6) In the model of the adult pike, dye appeared to pass through the posterior sensory channels (Figs. 7B, green disk, and 11F; Video clip 10). 7) Dye could be deflected dorsally by the nasal bridge (Fig. 11G; Video clip 11). (Video clip 11 guided our choice of the vorticity value that we used to define the thickness of the boundary layer; Section 2.7.3.) 8) In the model of the juvenile pike, dye passed over the excurrent nostril in a manner suggestive of another vortex (Fig. 11H, blue disk; Video clip 12). 9) Dye exiting the excurrent nostril passed over the lower part of the eye in the juvenile pike and under the eye in the adult pike (Figs. 11A, D – F, and A.8B, asterisks, Appendix A.5; Video clips 1, 4, 7, 9 and 10).

3.3. Computational fluid dynamics

3.3.1. General

The results from the CFD simulations were consistent with the dye visualisation experiments, indicating that the CFD results were valid. For example, dye behaviour in the flume could be replicated by streamlines generated from the CFD simulations (Fig. 11), including:

1) The rostral route taken by olfactory flow (Fig. 11B). 2) The two routes through the nasal chamber (Fig. 11D, Me and Lt). 3) The vortex in the incurrent nostril (Fig. 11E, blue disk). 4) Flow through the posterior sensory channels of the adult pike (Figs. 7B and 11F). 5) Deflection of flow over the nasal bridge (Fig. 11G). 6) The vortex in the excurrent nostril of the juvenile pike (Fig. 11H, blue disk).

The CFD simulations also showed that, as suggested by the dye visualisation experiments:

1) Flow decelerated in the nasal region (Fig. 12A, streamlines 1 and 2). 2) The anterior nasal region was a region of relatively high static pressure ($Cp > 0$; Fig. 13).

Additionally, the CFD simulations showed that:

1) The model's stagnation point was located on the rostral tip (Fig. 13, main images, white disks). 2) The anterior surface of the nasal bridge was a region of relatively high static pressure

(Fig. 13, insets). 3) The point of maximum pressure on the anterior surface of the nasal bridge (Fig. 13, insets, white disks) was located just lateral to its midline (Fig. 13A, inset, dashed yellow line). 4) This location was relatively insensitive to changes in the yaw angle (Fig. 13, insets, white disks; each white disk encompasses the point of maximum static pressure for each of the three different yaw angles, i.e. 0 ± 5°). 5) 38 – 40 % of the dynamic pressure of the external flow was harnessed by the nasal region in the juvenile pike, 26 – 29 % by the nasal region in the adult pike. 6) The incurrent vortex, the excurrent vortex, and the two routes through the nasal chamber persisted at different yaw angles (0 ± 5°; Fig. 12D). 7) Flow decelerated as it approached the nasal chamber floor (Fig. 14B and D). 8) The anterior part of the nasal chamber floor was a region of relatively high static pressure (Fig. 14A and C). 9) The anterior edge of the central posterior nasal fold (Fig. 14, yellow asterisks) was a region of particularly high static pressure (Fig. 14A and C, white disks). 10) Streamlines impinging on the centre of the olfactory rosette dispersed over the entire rosette (Fig. 14). 11) In general, these radially-dispersed streamlines passed along the sensory channels, including, as suggested in Section 3.2, the posterior sensory channels (Fig. 14, e.g. yellow arrows). Some radially-dispersed streamlines, however, passed *over* the nasal folds (Fig. 14, black asterisks). 12) The speed along the radially-dispersed streamlines in the incurrent nostril was relatively high (Fig. 15). 13) The vortex in the excurrent nostril in the juvenile pike (Fig. 12C, V2) could apparently entrain fluid from within the nasal chamber (Fig. 12C, blue streamlines). 14) Reynolds numbers in the nasal passage were 10 (juvenile pike) and 20 (adult pike). 15) The volumetric flow rate through the nasal chamber was 10 and 60 $mm^3\ s^{-1}$ (juvenile and adult pike, respectively – approximately three nasal chamber volumes s^{-1} for each model).

3.3.2. Boundary layer

We used CFD to define the boundary layer in the wild type and mutant models (Fig. 16, BL). (Wild type models had intact nasal regions; the nostrils and nasal chambers of the mutant models were replaced by a smooth surface; Section 2.4.) For the wild type models the boundary layer (Fig. 16B and D, blue regions) was for the most part superimposable on the boundary layer of the mutant models (the outer extent of which is indicated by each dashed black line in Fig. 16B and D). There was, however, a bulge over the excurrent nostril in the boundary layer of each wild type model (Fig. 16B and D, asterisks). The extent of the bulge correlated with the extent to which the nasal bridge protruded from the surface of the head. Thus the bulge was greater in the wild type model of the adult pike (Fig. 16D, asterisk). The

boundary layer above the dorsal edge of the nasal bridge was comparatively thinner for the wild type model of the adult pike (Fig. 16D). In neither wild type model (juvenile or adult) did the nasal bridge protrude from the boundary layer (Fig. 16B and D).

We also found that free-stream flow sampled by the nasal chamber entered the boundary layer near the rostral tip (Fig. 16A and C, yellow regions). The time taken (*t*, Fig. 16A and C) for a fluid particle travelling along a streamline to get from its point of entry into the boundary layer to the incurrent nostril varied from 0.2 to 1.8 s in the juvenile pike and 0.3 to 3.1 s in the adult pike. The time taken for external flow to travel the horizontal distance from the rostral tip to the centre of the incurrent nostril was 0.1 s (juvenile pike) and 0.3 s (adult pike). The maximum delay caused by the boundary layer was therefore 1.7 s (juvenile pike) and 2.8 s (adult pike).

3.3.3. Drag

We also used CFD to determine the drag incurred by the models of the pike's head, including the contributions to the overall drag of pressure drag and viscous drag (Shapiro, 1961, p. 81). The results were similar for both the juvenile and the adult pike (Table 1). Viscous drag was the major contributor (76 – 86 %) to the total drag of each model (Table 1, grey entries), suggesting that the models were streamlined (Massey, 1989, p. 255), and that the artificial tail (Fig. A.4, Appendix A.5) prevented separation at the back of the head, thereby fulfilling its intended function (Appendix A.1.7.1). In the mutant models, the nasal regions contributed 5.3 or 3.6 % (first percentage here and below: juvenile pike; second percentage: adult pike) to the total drag (Table 1, yellow entries). The nasal regions of the wild type models made almost the same contribution to the total drag (5.4 or 4.0 %; Table 1, gold entries) as the nasal regions of the mutant models. Thus, for the wild type and mutant models derived from the same specimen (e.g. the juvenile pike), the contribution of the nasal regions to the total drag of the wild type model was only 0.1 or 0.4 % greater than that of the nasal region of the mutant model. Viscous drag made only a small contribution (12 – 23 %; Table 1, blue entries) to the total drag of the nasal regions in both the wild type and the mutant models.

4. Discussion

4.1. Flow through the pike's nasal chamber is induced by an external flow

We showed that flow of water through the nasal chamber of the pike can be induced by an external flow at physiologically relevant Reynolds numbers (200 – 300). *In vivo*, the origin of the external flow may be a water current in one of the pike's varied habitats (e.g. lake, stream, or river; Masters et al., 2002) or the movement of the pike as it swims forward (e.g. when moving from one habitat to another; Chapman and Mackay, 1984; Masters et al., 2002).

4.2. Age-related differences in the pike's nasal anatomy

The principal differences between the nasal anatomy of the juvenile and adult pike are: 1) the nasal region of the adult pike is larger than that of the juvenile pike; 2) the dorsal edge of the nasal bridge protrudes more from the surface of the adult pike's head (cf. asterisked sections, Fig. 8); 3) the complementary interaction between the ventral surface of the nasal bridge and the central posterior nasal fold is more marked in the juvenile pike (cf. Fig. 9A and B); and 4) the nasal folds are more pronounced in the adult pike (cf. Fig. 14B and D). We discuss in the ensuing sections how these differences influence both olfactory flow and odorant transport. Because the differences may offset one another, we do not state whether overall they might have benefitted *in vivo* one specimen more than the other.

4.3. Key elements in the pike's olfactory flow

Olfactory flow in the pike comprises four key elements (summarised in Fig. 17):

1) Flow deflected dorsally and ventrally by the nasal bridge (Fig. 12A, streamlines 1 and 2, and Fig. 17, red disk and arrow).

2) Flow dispersed on the nasal chamber floor (Fig. 14, and Fig. 17, white disk).

The origins of flow elements 1) and 2) are discussed in Sections 4.4 and 4.6, respectively.

3) A vortex in the incurrent nostril ('incurrent vortex'; Figs. 12B and 17, V1; Video clips 8 and 9). The incurrent vortex is likely to arise when flow passing over the anterior rim of the incurrent nostril separates from the surface of the head. Separation occurs because the surface suddenly expands at this point (Chang, 1976, p. 3). The sudden expansion causes an adverse

pressure gradient, which in turn causes flow to reverse and a vortex to form (Fox, 1974, p. 163). A rearward-facing step, a curved wall, and a sudden enlargement in a pipe have similar effects on flow (Fig. 6.16 of Fox, 1974; Fig. 1.4a of Chang, 1976; Fig. 38 of Van Dyke, 1982).

4) A vortex in the excurrent nostril ('excurrent vortex'; Figs. 12C and 17, V2, inset; Video clip 12). The excurrent vortex is present in the olfactory flow of the juvenile pike only. It occupies the medial part of the excurrent nostril (Fig. 12C, yellow streamlines). Formation of the excurrent vortex is likely to arise in the same manner as the incurrent vortex, with external flow separating as it passes over the medial rim of the excurrent nostril (Fig. 12C, blue asterisk). A shallow cavity has a similar effect on flow (Fig. 1.4b of Chang, 1976; Fig. 14 of Van Dyke, 1982). The absence of an excurrent vortex in the adult pike is presumably due to the more dorsally extended nasal bridge (Fig. 12A, circle), which may prevent external flow passing directly over the medial part of the excurrent nostril.

All four flow elements persisted at different yaw angles ($0 \pm 5°$) in the CFD simulations (e.g. Fig. 12D, V1).

4.4. Factors determining externally-induced flow through the nasal chamber

Externally-induced flow through the nasal chamber may be attributed to:

1) The location of the incurrent nostril in a region of relatively high static pressure ($Cp > 0$; Fig. 13). The relatively high static pressure in this region will force flow into the nasal chamber.

2) The nasal bridge impeding external flow. The nasal bridge is both fully exposed to the oncoming external flow (Fig. 13, insets) and normal to this flow (Fig. 8, vertical arrows). Consequently, it will act like a flat plate normal to flow (Schlichting, 1960, p. 33; Fig. I.4 of Thwaites, 1960; Fig. 10.4b of Douglas et al., 1985), deflecting flow a) under its ventral edge and into the nasal chamber, and b) over its dorsal edge (Fig. 17, red arrow). The idea that the nasal bridge deflects flow into the pike's nasal chamber was suggested by Burne (1909).

Because the nasal bridge impedes flow, it is a region of particularly high static pressure (Fig. 13, insets, area between dashed black lines). The point of highest pressure on the nasal bridge

(just lateral to its midline; Fig. 13, insets, white disks) is consistent with the direction from which rostral flow approaches the nasal region (Fig. 11B). The invariance of this location with yaw (Fig. 13, insets, white disks) explains why the key olfactory flow elements persist at different yaw angles (Fig. 12D). This invariance also suggests that flow through the nasal chamber will occur even if a stationary pike is not directly facing an oncoming water current, a situation that might arise when it is waiting to ambush prey (Wheeler, 1969, pp. 166-167).

The nasal bridge's ability to impede flow is no doubt aided by the fact that it is fairly rigid. Thus, the nasal bridges of the two preserved specimens resisted gentle pushing with blunt-ended tweezers (the nasal bridges behaved like durable foam, returning to their original shape after being pushed). Admittedly this resistance may have been due to several decades of storage in preservative fluid. Any rigidity in the specimens' nasal bridges *in vivo* must have stemmed from the nasal morphology, because these nasal bridges were not supported by cartilage. Thus, there are in the micro-CT scans no intense pixels (indicative of cartilage) in the nasal bridge regions (Fig. 2, NB). Cartilage is, however, present in the nasal bridges of older specimens (Holl, 1965). We also noted that the dorsal edges of the nasal bridges of the aquarium specimens were not deflected when these specimens swam forwards.

3) The excurrent nostril lying normal to the external flow (Fig. 8, vertical arrows). As a result, the fluid within the excurrent nostril should experience only the ambient static pressure of the external flow (Vogel, 1994, p. 60), thereby creating a positive pressure difference across the nostrils. In fact, the static pressure of the fluid within the excurrent nostril was very close to ambient static pressure ($Cp \sim 0 - 0.1$).

4) Viscous entrainment (Cox, 2008). Fluid may be drawn *into* the nasal chamber (Fig. 17, dashed yellow circle) by the tractive viscous forces applied to it by the incurrent vortex (Fig. 17, V1) and by flow deflected ventrally by the nasal bridge (Fig. 17, red arrow). Fluid may be drawn *out of* the nasal chamber (e.g. Fig. 17, white arrow) by the tractive viscous forces applied to it by external flow passing directly over the excurrent nostril (Fig. 17, red arrow). The effect of the nasal bridge, which protrudes from the surface of the head (Fig. 8, asterisked sections), is to accelerate flow in this region (resulting in a thinner boundary layer here than for the mutant models; Fig. 16B and D), thereby increasing these tractive viscous forces. (In the mutant models, the nostrils and nasal chambers were replaced by a smooth surface.) The tractive viscous forces are likely to be greater in the adult pike than in the

juvenile pike because the adult pike's nasal bridge protrudes dorsally to a greater extent than the juvenile's (cf. asterisked sections, Fig. 8). Consequently, there will be at this point a thinner boundary layer (cf. Fig. 16B and D). In the juvenile pike, fluid may also be drawn from the nasal chamber (Fig. 17, yellow arrow, inset) by the excurrent vortex (Fig. 17, V2, inset).

4.5. Other mechanisms that may generate flow through the nasal chamber

Two other ways in which flow through the pike's nasal chamber may be generated are: 1) by the co-ordinated beating of the non-sensory cilia (Reiten et al., 2017) on the nasal folds (Fig. 30 of Holl, 1965); and 2) when water is drawn into the mouth during respiration. Our inanimate plastic models did not allow us to investigate ciliary-driven flow, so this remains a possibility in the pike. From our observations of the aquarium specimens, however, we conclude that respiration is unlikely to assist flow through the pike's nasal chamber. Thus, although the mouths of these specimens remained slightly open when they cruised, we could see no independent movements of their jaws. When the pike were stationary, their mouths were again slightly open, and there were small movements of their jaws, particularly the lower jaw, but we thought these movements were not sufficient to cause flow through the nasal chamber.

4.6. Dispersal of flow over the olfactory sensory surface

Flow may be dispersed over the pike's olfactory sensory surface by:

1) Impaction on the nasal chamber floor. Relatively high-speed incurrent flow (Fig. 15) decelerates as it approaches the centre of the olfactory rosette, leading to radial dispersal of flow over the entire nasal chamber floor, particularly in the sensory channels (Fig. 14B and D). As a result of the impact, the anterior part of the nasal chamber floor is a region of relatively high static pressure (Fig. 14A and C). It is probably not a coincidence that the centre of the olfactory rosette (Fig. 7, black disks) is located where the relatively high-speed incurrent flow strikes the nasal chamber floor. Impact-driven dispersal may be aided by the radially-arranged nasal folds acting as guides to flow (Fig. 14). The nasal folds are more pronounced in the adult pike (cf. Fig. 14B and D), and should therefore be better guides than the nasal folds in the juvenile pike. Flow over the nasal chamber floor is not, however, entirely constrained by the nasal folds: it can also pass *over* them (Fig. 14, black asterisks).

The dispersal of flow over the pike's olfactory rosette by impaction is reminiscent of a jet of fluid spreading over a surface it strikes (Massey, 1989, p. 117).

2) The central posterior nasal fold. The central posterior nasal fold (Fig. 14, yellow asterisks) splits flow in the nasal passage into a lateral stream and a medial stream (Fig. 14, yellow arrows; see also Video clips 6 and 7). A region of relatively high static pressure on the anterior edge of the central posterior nasal fold (Fig. 14A and C, white disks) testifies to this fold's flow-splitting role. The division of flow into two streams may be assisted by the complementary interaction between the central posterior nasal fold and the ventral surface of the nasal bridge (Fig. 9). This interaction is particularly noticeable in the juvenile pike (cf. Fig. 9A and B).

3) The incurrent vortex. The incurrent vortex directs flow a) over the *anterior* section of the nasal chamber floor (opposite to the direction of the free-stream flow; Fig. 17, arrow 1) and b) through the medial section of the nasal passage (Fig. 12B).

4.7. The influence of the boundary layer on odorant transport

The boundary layer may delay odorant transport from the external environment to the nasal region of a fish (Denny, 1993, p. 138). The delay for the pike may be considerable (up to ~ 3 s). Such long delays may be (unavoidably) detrimental to its olfactory abilities. The maximum delay for the adult pike is probably longer than that for the juvenile pike because the rostrum of the adult pike is blunter than that of the juvenile's (cf. Fig. 1C and D, arrowheads).

4.8. The drag incurred by the nasal region

The drag incurred by the nasal region of the wild type models (nasal region intact) is almost the same as the drag incurred by the nasal region of the mutant models (nostrils and nasal chamber replaced by a smooth surface). Thus olfactory sampling in the pike may be achieved whilst incurring little additional drag (relative to the mutant head).

The relatively small contribution (~ 10 – 25 %) of viscous drag to the total drag of the nasal region of the wild type models can be explained as follows. Substantial parts of the nasal bridge and the nasal passage are normal to flow (Fig. 8). The viscous forces experienced by

flow in these regions will therefore be normal to external flow (Fig. 17, arrows 2 – 4) and should therefore not contribute greatly to viscous drag. On the other hand, the viscous forces associated with that part of the flow in the incurrent vortex moving in an *anterior* direction (Fig. 17, V1 and arrow 1) should provide (an extremely small) *thrust*. It is noteworthy that the viscous drag in the nasal region of a wild type model matches or is almost identical to that of the corresponding mutant model (Table 1, blue entries) even though the surface area of the nasal region of the wild type model is approximately twice that of the mutant model.

Crucially, the boundary layer in the nasal region of the wild type models remains attached to the surface of the head (Fig. 16B and D). If the boundary layer separated, a wake would form, leading to increased drag (Massey, 1989, p. 255). Separation of the boundary layer can only occur in the presence of *both* an adverse pressure gradient *and* adverse viscous forces (Chang, 1970, p. 5). The boundary layer *cannot* separate if one of these influences is absent. Separation of the boundary layer in the nasal region of the pike is avoided because:

1) Flow accelerates over the dorsal edge of the nasal bridge, as evidenced by the thin boundary layer and condensed isotachs (lines of equal flow speed; Vogel, 1994, p. 45) in this region (Fig. 16B and D, round insets). In other words, there is a favourable pressure gradient here, and therefore the boundary layer cannot separate.

2) Flow striking the nasal bridge experiences an adverse pressure gradient but *not* adverse viscous forces. Adverse viscous forces are reduced because the viscous forces associated with flow that has been deflected dorsally and ventrally over the surface of the nasal bridge are largely *normal* to the external flow (Fig. 17, arrows 2 and 3). In the absence of substantial adverse viscous forces, the boundary layer cannot separate.

3) The nasal bridge may be streamlined (Kaufmann, 1974, pp. 6-7). The nasal bridge is tapered in sagittal cross-section, with a rounded ventral edge and a thinner, but still rounded, dorsal section (Fig. 8), not unlike an aerofoil (Fig. 10.16 of Douglas et al., 1985). Indeed, flow in the vicinity of the nasal bridge's dorsal edge behaves like flow passing over the trailing edge of an aerofoil. For example, streamlines deflected dorsally and ventrally by the nasal bridge meet and depart smoothly from its dorsal edge (Figs. 12A, asterisk, and 17, red arrow). They do not form a wake (cf. Fig. 10c of Goldstein, 1965).

4) Separated flow is controlled. Flow becomes separated from the surface of the head at two locations in the nasal region. One location is the dorsal edge of the nasal bridge (Fig. 17, red arrow). As described in 3) above, no wake is formed here. The other location is the rim of the incurrent nostril (Fig. 17, IN). Part of this separated flow forms the incurrent vortex (Fig. 17, V1). Although a vortex could potentially form a wake (Fig. 10.26 of Douglas et al., 1985), it does not do so here because it is effectively destroyed when it passes through the nasal passage (Fig. 12B). The other part of the flow that separates from the rim of the incurrent nostril becomes reattached either to the nasal bridge (Fig. 17, red disk) or to the nasal chamber floor (Fig. 17, white disk), or it passes through the nasal chamber (Fig. 17, yellow arrow). Reattachment to the nasal chamber floor serves to trap partly the incurrent vortex as a separation bubble (Fig. 37 of Chang, 1970). Reattachment of flow to the nasal bridge may be aided by the relatively narrow spacing between the nasal bridge and the rim of the incurrent nostril (Panton, 1984, p. 541). Thus, although flow *does* separate from the surface of the head in the nasal region, it does *not* lead to the separation of the boundary layer.

Evidence that the boundary layer remains attached to the nasal region of the pike *in vivo* came from an observation of one of the aquarium specimens. This specimen had a fine thread attached to its left nasal bridge. When the specimen swam, the thread trailed without wavering. (A wavering thread would have indicated separation.)

4.9. Other aspects of olfactory flow

Reynolds numbers in the nasal chamber are low (10 – 20). Viscous forces here are, therefore, relatively large (Shapiro, 1961, p. 78). The viscous nature of flow in the nasal chamber is evident from the absence of separation when flow passes over, rather than along, the nasal folds (Fig. 14, black asterisks). The floor of the nasal chamber may therefore be considered hydrodynamically smooth (Shapiro, 1961, p. 121), despite the presence of the nasal folds.

The incurrent vortex may encourage odorant transport to the olfactory sensory surface by bringing several times the same fluid particle into proximity with the surface (Fig. 12B, inset, blue disks). Thus, the incurrent vortex may allow the fluid to be resampled by the olfactory sensory surface. Olfactory resampling may also occur in the European eel (*Anguilla anguilla*; Teichmann, 1959).

4.10. Comparison with externally-induced olfactory flow in the sturgeon

Externally-induced olfactory flow in the pike is similar in several ways to that in the sturgeon, *Huso dauricus* (Garwood et al., 2019):

1) Both the pike and the sturgeon have an incurrent nostril located in a region of relatively high static pressure, where flow will be forced into the nasal chamber.

2) Both fishes have a feature that impedes external flow, deflecting it into the nasal chamber. In the sturgeon this feature is the lateral wall of the incurrent nostril. In the pike, it is the nasal bridge.

3) Both fishes have an excurrent nostril normal to external flow. Consequently, in both fishes the fluid in the excurrent nostril experiences a static pressure equal or close to the ambient static pressure of the external flow.

4) In both the pike and the sturgeon, flow is dispersed over the olfactory sensory surface by a jet impingement-like mechanism. Specifically, dispersal occurs when relatively high speed incurrent flow decelerates on encountering an internal nasal surface (the central support in the sturgeon; the nasal chamber floor in the pike).

5) Vortices may assist olfaction in both fishes. Vortices in the nasal chamber of the sturgeon, like those in the pike, may assist flow through the nasal chamber by viscous entrainment.

Furthermore, the percentage of the dynamic pressure of the free-stream flow harnessed by the nasal regions of both fishes is similar (pike: ~ 25 – 40 %; sturgeon: ~ 35 %). The dye visualisation experiments suggested, however, that the sturgeon's nasal region is better at harnessing external flow than the pike's. Thus, in the dye visualisation experiments with the sturgeon model, the dye filament passed largely intact into the incurrent nostril (e.g. Video clip 1 of Garwood et al., 2019). With the pike models, however, not all the dye impinging on the incurrent nostril passed into it (e.g. Video clip 2). Furthermore, in the CFD simulations of olfactory flow in the juvenile pike, a streamline that impacted on the nasal chamber floor could subsequently pass *out* of the incurrent nostril (Fig. 14A and B, black arrows).

The sturgeon's nasal region may appear to be better at harnessing external flow than the pike's because the fluid dynamics experiments with the sturgeon models were performed at higher Reynolds numbers than those with the pike models (500 *v.* 200 – 300, respectively). We note also that the sturgeon's excurrent nostril is in a region of low static pressure ($Cp < 0$), where there will be a tendency for flow to be drawn out of it. The pike's excurrent nostril, on the other hand, is essentially in a region where $Cp > 0$ (Fig. 13). In addition, the sturgeon's excurrent nostril is three times larger than its incurrent nostril, whereas the pike's excurrent nostril is about the same size as its incurrent nostril. Viscous entrainment of flow from the sturgeon's excurrent nostril may therefore be more effective than from the pike's (Vogel, 1978).

4.11. Limitations

Many of the limitations of the current study (and, where possible, their mitigation) are common to our previous studies (Abel et al., 2010; Agbesi et al., 2016a, 2016b; Garwood et al., 2019), and are discussed therein (see also Appendix A.3). One limitation of note in the current study was the lack of convexity in the eyes of the models of the juvenile pike (Fig. 3A). *In vivo*, as we observed in the aquarium and survey specimens, the eyes of the pike are convex. In the preserved specimens on which our models are based, only the adult pike had convex eyes. The eyes of the preserved specimen of the juvenile pike had collapsed to a flattened state. We were, therefore, able only to capture the convexity of the pike's eyes in the models of the adult pike specimen (Fig. 3B). We found, however, that this convexity had only a minor effect on olfactory flow. Thus, in the models of the adult pike, flow passed under the eye (Fig. 11, asterisks; e.g. Video clip 1), whereas in the models of the juvenile pike, flow typically passed over the ventral part of the eye, not under it (Fig. A.8B, asterisk, Appendix A.5; Video clip 4). But, except for the excurrent vortex in the juvenile pike, the key olfactory flow elements in the models of the juvenile and adult pike were similar (cf. Video clips 8 and 9, for example).

The other limitation of note in the current study was our failure to include in our models the transverse nasal folds of the pike's olfactory rosette (Fig. 1F, inset, yellow disk; see also Fig. 27 of Holl, 1965). We were able to see (e.g. with a stereomicroscope) the transverse nasal folds of the preserved specimens of the juvenile and adult pike (they gave the olfactory rosette a cribriform appearance; Fig. 1F), but the micro-CT scan of each head did not resolve them. (This inability was not due to the quality of the scans: the voxel size of each scan was

733 limited by the size of the head.) Nevertheless, given that the floor of the nasal region may be
734 considered hydrodynamically smooth (Section 4.9), we believe that inclusion of the
735 transverse nasal folds would not have significantly affected the key olfactory flow elements.
736

5. Conclusion

The nasal bridge and a vortex in the incurrent nostril play multiple roles in olfactory flow in the pike, with several probable benefits for olfaction. Both features may facilitate odorant transport by a) encouraging flow through the nasal chamber and b) dispersing flow over the olfactory sensory surface. At the same time, drag (and therefore the metabolic cost to the fish) is minimised. The nasal bridge encourages flow through the nasal chamber by obstructing (via its anterior surface) and accelerating (via its dorsal edge) local external flow. In addition, the nasal bridge may encourage dispersal of flow over the olfactory sensory surface by diverting it (via a complementary interaction between its ventral surface and the central posterior nasal fold) medially and laterally within the nasal chamber. The nasal bridge minimises drag by its orthogonality to external flow, by its streamlined shape, and by accelerating (again via its dorsal edge) local external flow. The incurrent vortex, which arises as a result of the *provoked* separation of local external flow (via the sudden expansion of the surface of the head), may encourage flow into the nasal chamber by viscous entrainment. Fluid motion within the incurrent vortex encourages dispersal of flow over the anterior olfactory sensory surface, which at the same time may contribute to (a small) thrust, thereby minimising drag. The incurrent vortex may also encourage odorant transport to the olfactory sensory surface by bringing several times the same fluid particle into contact with that surface. In short, the pike's apparently simple nasal anatomy belies a remarkable piece of natural engineering.

Acknowledgements

We thank: Laser Lines/Ogle Models and Prototypes for 3D printing; Brecht Morris (Environment Agency, UK) and Robert Britton (University of Bournemouth, UK) for allowing JPLC to observe the pike they caught during a joint Environment Agency/University of Bournemouth survey; the staff of the Aquarium of the Lakes, Cumbria, UK, for facilitating our other observations of pike *in vivo*; Celia Butler, Matt Cross, Paul Frith, Graham Martin, and Simon Wharf for technical assistance; Ismet Gursul and Richie Gill for allowing us to use, respectively, the flume and the ScanIP software in the Department of Mechanical Engineering at Bath; Kevin Webb and Harry Taylor for photography; David Cleaver, Oliver Crimmen, and Jos Darling for helpful discussions; Mawuli Agbesi and Flo Lendrum for contributing to the initial fluid dynamics experiments on the models of the juvenile pike; Xavier Mear for German to English translation, and Asel Sartbaeva for Russian to English translation.

Funding statement

This work was supported by the University of Bath's Alumni Fund. The Engineering and Physical Sciences Research Council, UK, funded the Henry Moseley X-ray Imaging Facility through the Royce Institute for Advanced Materials (grants EP/F007906/1, EP/F001452/1, EP/I02249X, EP/M010619/1, EP/F028431/1, EP/M022498/1 and EP/R00661X/1). The funding sources were not involved in the conduct of the research, or the preparation of the article.

780 **References**

781 Abel, R.L., Maclaine, J.S., Cotton, R., Xuan, V.B., Nickels, T.B., Clark, T.H., Wang, Z.,
782 Cox, J.P.L., 2010. Functional morphology of the nasal region of a hammerhead shark. Comp.
783 Biochem. Physiol. A 155, 464-475.
784 Abernathy, F.H., 1972. Fundamentals of boundary layers. In: National Committee for Fluid
785 Mechanics Films. Illustrated Experiments in Fluid Mechanics. MIT Press, London, pp. 75-81.
786 Agbesi, M.P.K., Naylor, S., Perkins, E., Borsuk, H.S., Sykes, D., Maclaine, J.S., Wang, Z.,
787 Cox, J.P.L., 2016a. Complex flow in the nasal region of guitarfishes. Comp. Biochem.
788 Physiol. A 193, 52-63.
789 Agbesi, M.P.K., Borsuk, H.S., Hunt, J.N., Maclaine, J.S., Abel, R.L., Sykes, D., Ramsey
790 A.T., Wang, Z., Cox, J.P.L., 2016b. Motion-driven flow in an unusual piscine nasal region.
791 Zoology 119, 500-510.
792 Ayachit, U., 2016. The ParaView Guide. Kitware Inc.
793 Barnard, R.H., Philpott, D.R., 2004. Aircraft Flight. 3rd ed. Pearson Education, Harlow.
794 Barnard, R.H., 2009. Road Vehicle Aerodynamic Design. 3rd ed. MechAero Publishing, St
795 Albans.
796 Burne, R.H., 1909. The anatomy of the olfactory organ of teleostean fishes. Proc. Zool. Soc.
797 Lond. 2, 610-663.
798 Chang, P.K., 1970. Separation of Flow. Pergamon Press, Oxford.
799 Chang, P.K., 1976. Control of Flow Separation. Hemisphere, Washington.
800 Chapman, C.A., Mackay, W.C., 1984. Versatility in habitat use by a top aquatic predator,
801 *Esox lucius* L. J. Fish Biol. 25, 109-115.
802 Cox, J.P.L., 2008. Hydrodynamic aspects of fish olfaction. J. Roy. Soc. Interface 5, 575-593.
803 Craig, J.F., 1996. Pike. Chapman & Hall, London.
804 Craig, J.F., 2008. A short review of pike ecology. Hydrobiologia 601, 5-16.
805 Denny, M.W., 1993. Air and Water. Princeton University Press, Princeton.
806 Devitsina, G.V., Malyukina, G.A., 1977. The functional organisation of the olfactory organ in
807 macrosomatic and microsomatic fishes. Ichthyol. Questions 17, 493-502. In Russian.
808 Douglas, J.F., Gasiorek, J.M., Swaffield, J.A., 1985. Fluid Mechanics. 2nd ed. Pitman,
809 Massachusetts.
810 Fox, J.A., 1974. An Introduction to Engineering Fluid Mechanics. Macmillan, London.
811 Fox, R.W., McDonald, A.T., Pritchard, P.J., Leylegian, J.C., 2012. Fluid Mechanics. 8th ed.
812 John Wiley & Sons, Asia.

Garwood, R.J., Behnsen, J., Haysom, H.K., Hunt, J.N., Dalby, L.J., Quilter, S.K., Maclaine, J.S., Cox, J.P.L., 2019. Olfactory flow in the sturgeon is externally driven. Comp. Biochem. Physiol. A 235, 211-225.

Garwood, R.J., Behnsen, J., Maclaine, J.S., Cox, J.P.L., 2020a. TIFF images from X-ray scan of head of *Esox lucius* (adult). Mendeley Data, v1. http://dx.doi.org/10.17632/bgv6gs9dvr.1.

Goldstein, S., 1965. Modern Developments in Fluid Dynamics. Dover Publications, New York.

Haynes, W.M., Lide, D.R., 2011. CRC Handbook of Chemistry and Physics. 92nd ed. CRC Press, Boca Raton.

Haysom, H.K., Quilter, S.K., Dalby, L.J., Cox, J.P.L., 2019. STL models of heads of *Esox lucius*. Mendeley Data, v1. http://dx.doi.org/10.17632/hv4xjnzrnf.1.

Helfman, G.S., Collette, B.B., Facey, D.E., Bowen, B.W., 2009. The Diversity of Fishes. 2nd ed. Wiley-Blackwell, Chichester.

Holl, A., 1965. Vergleichende Morphologische und Histologische Untersuchungen am Geruchsorgan der Knochenfische (Comparative morphological and histological investigations on the olfactory organ of bony fishes). Z. Morph. Ökol. Tiere 54, 707-782. In German.

Holmes, W.M., Cotton, R., Xuan, V.B., Rygg, A.D., Craven, B.A., Abel, R.L., Slack, R., Cox, J.P.L., 2011. Three-dimensional structure of the nasal passageway of a hagfish and its implications for olfaction. Anat. Rec. 294, 1045-1056.

Howard, L.E., Holmes, W.M., Ferrando, S., Maclaine, J.S., Kelsh, R.N., Ramsey, A., Abel, R.L., Cox, J.P.L., 2013. Functional nasal morphology of chimaerid fishes. J. Morph. 274, 987-1009.

Kaufmann, J., 1974. Streamlined. Thomas Y. Crowell Company, New York.

Kline, S.J., 1972. Flow visualization. In: National Committee for Fluid Mechanics Films. Illustrated Experiments in Fluid Mechanics. MIT Press, London, pp. 34-38.

Lugt, H.J., 1983. Vortex Flow in Nature and Technology. John Wiley & Sons, New York.

Massey, B.S., 1989. Mechanics of Fluids. 6th ed. Van Nostrand Reinhold, London.

Masters, J.E.G., Welton, J.S., Beaumont, W.R.C., Hodder, K.H., Pinder, A.C., Gozlan, R.E., Ladle, M., 2002. Habitat utilisation by pike *Esox lucius* L. during winter floods in a southern English chalk river. Hydrobiologia 483, 185-191.

Nelson, J.S., 2006. Fishes of the World. 4th ed. John Wiley & Sons, New Jersey.

Panton, R.L., 1984. Incompressible Flow. John Wiley & Sons, New York.

Raat, A.J.P., 1988. Synopsis of Biological Data on the Northern Pike, *Esox lucius* Linnaeus, 1758. FAO Fisheries Synopsis No. 30 Rev. 2. Food and Agriculture Organization of the United Nations, Rome.

Ramsey, A., Houston, T.F., Ball, A.D., Goral, T., Barclay, M.V.L., Cox, J.P.L., 2015. Towards an understanding of molecule capture by the antennae of male beetles belonging to the genus *Rhipicera* (Coleoptera, Rhipiceridae). Anat. Rec. 298, 1519-1534.

Ramsey, A.T., Maclaine, J.S., Cox, J.P.L., 2020. TIFF images from X-ray scan of head of *Esox lucius* (juvenile). Mendeley Data, v1. http://dx.doi.org/10.17632/g5vx38jh5j.1.

Reiten, I., Uslu, F.E., Fore, S., Pelgrims, R., Ringers, C., Verdugo, C.D., Hoffman, M., Lal, P., Kawakami, K., Pekkan, K., Yaksi, E., Jurisch-Yaksi, N., 2017. Motile-cilia-mediated flow improves sensitivity and temporal resolution of olfactory computations. Curr. Biol. 27, 166-174.

Schlichting, H. 1960. Boundary Layer Theory. McGraw-Hill, New York.

Shapiro, A.H., 1961. Shape and Flow. Heinemann, London.

Shapiro, A.H., 1972. Pressure fields and fluid acceleration. In: National Committee for Fluid Mechanics Films, Illustrated Experiments in Fluid Mechanics. MIT Press, London, pp. 39-46.

Teichmann, H., 1954. Vergleichende Untersuchungen an der Nase der Fische (Comparative studies on the nose of the fish). Z. Morph. Ökol. Tiere 43, 171-212. In German.

Teichmann, H., 1959. Über die Leistung des Geruchssinnes beim Aal [*Anguilla anguilla* (L.)] (On the performance of the sense of smell of the eel). Z. vgl. Physiol. 42, 206-254. In German.

Theisen, B., 1982. Functional morphology of the olfactory organ in *Spinachia spinachia* (L.) (Teleostei, Gasterosteidae). Acta Zool. 63, 247-254.

Thwaites, B., 1960. Incompressible Aerodynamics. Clarendon Press, Oxford.

Van Dyke, M., 1982. An Album of Fluid Motion. The Parabolic Press, Stanford.

Vogel, S., 1978. Organisms that capture currents. Sci. Am. August, 108-117.

Vogel, S., 1988. How organisms use flow-induced pressures. Am. Sci. 76, 28-34.

Vogel, S., 1994. Life in Moving Fluids. 2nd ed. Princeton University Press, Princeton.

Wang, Z.-J., Jiang, P., Gursul, I., 2007. Effect of thrust-vectoring jets on delta wing aerodynamics. J. Aircraft 44, 1877-1888.

Webb, P.W., 1984. Form and function in fish swimming. Sci. Am. July, 72-82.

Weller, H.G., Tabor, G., Jasak, H., Fureby, C., 1998. A tensorial approach to computational continuum mechanics using object-oriented techniques. Comp. Phys. 12, 620-631.

Wheeler, A., 1969. The Fishes of the British Isles and North-West Europe. Macmillan, London.

880 Zeiske, E., Theisen, B., Breucker, H., 1992. Structure, development, and evolutionary aspects
881 of the peripheral olfactory system. In: Hara, T.J. (Ed.), Fish Chemoreception. Chapman &
882 Hall, London.
883

884 **Figure legends**

885

886 **Fig. 1** The two pike (*Esox lucius*) specimens used to generate the fluid dynamics models. (A),
887 (C) and (E): Juvenile pike (BMNH 1963.4.26.2). (B), (D) and (F): Adult pike (BMNH
888 1986.5.20.4). (A) and (B): Complete specimens; (C) and (D): heads; (E) and (F): superior
889 view of each nasal region. Inset in (D): magnified nasal region. Inset in (F): magnified yellow
890 highlighted section, main image. White regions in inset (F): location of sensory olfactory
891 epithelium. Yellow disk in inset (F): transverse fold. Specimen in (B) and (D) outlined in
892 white to improve contrast with background. Nostrils filled in black in (C), for emphasis.
893 Arrowheads in (C) and (D): anterior rostral edge. White marks, panel frames (A) – (D):
894 posterior extent of X-ray scan (A and B); location of TIFF images shown in Fig. 2 (C and D).
895 Yellow marks in (D): location of TIFF image, Fig. A1.C, Appendix A.5. a: Anterior; AF:
896 anal fin; EN: excurrent nostril; *FL*: fork length (distance from rostral tip to asterisk); IN:
897 incurrent nostril; l: lateral; m: medial; NB: nasal bridge (extent indicated by dashed black
898 lines); NR: nasal region; p: posterior; PF: pectoral fin; Ro: rostrum.

899

900 **Fig. 2** TIFF images from micro-CT scans of (A) juvenile and (B) adult pike. Transverse
901 cross-section through each head (location indicated in Fig. 1C and D, respectively). Yellow
902 line: perimeter of nasal chamber. Ai: Air; Bo: bone; d: dorsal; NB: nasal bridge; OC: oral
903 cavity; Ti: tissue; v: ventral.

904

905 **Fig. 3** Surface models of heads of (A) juvenile and (B) adult pike. Insets: magnified nasal
906 region. Dashed lines in insets: limits of nasal bridge. Positive and negative yaw angles
907 indicated by red and blue arrows, respectively. EN: Excurrent nostril; Ey: eye; IN: incurrent
908 nostril; NR: nasal region.

909

910 **Fig. 4** Plastic models of heads of (A) juvenile and (B) adult pike. Insets: magnified nasal
911 region. Black lines in insets: extent of nasal chamber. EN: Excurrent nostril; Ey: eye; IN:
912 incurrent nostril; NR: nasal region; Op: opaque part; PF: pectoral fin; Tr: translucent part.

913

914 **Fig. 5** CFD mesh of adult pike. (A) Refinement of mesh on model surface, nasal region
915 (superior view). Large circles: magnified border (small circles) at two stages of refinement,
916 with refinement increasing bottom to top. (B) Transverse cross-section through mesh (same

cross-section as in Fig. 2B). (C) Transverse cross-section through nasal passage. Inset in (C): mesh next to olfactory sensory surface (asterisked box, main image). The seams (e.g. Se) in (C) are artifacts arising from the way ParaView's Slice filter cuts a mesh. Scale bars in (A) and (B) and labels in all images deliberately omitted to allow reader to see mesh. a: Anterior; d: dorsal; l: lateral; m: medial; p: posterior; Se: seam; v: ventral.

Fig. 6 Characteristic dimension of adult pike's nasal region. (A) Head of surface model, right half, dorsal aspect. (B) Highlighted nasal region in (A), dorsal aspect. Arrow: direction of free-stream flow. a: Anterior; EN: excurrent nostril; IN: incurrent nostril; *L*: characteristic dimension of nasal region; l: lateral; m: medial; NR: nasal region; p: posterior.

Fig. 7 Detail of surface models of (A) juvenile and (B) adult pike. Superior views of nasal region. Arrow: direction of free-stream flow. Asterisk: central posterior nasal fold. Black disk: centre of olfactory rosette. Green disk: sensory channel. Yellow marks, panel frames: positions of sagittal sections in Figs. 8, 16B, D, and 17. Black marks, panel frames: position of transverse sections in Fig. 9. a: Anterior; EN: excurrent nostril; IN: incurrent nostril; l: lateral; m: medial; NB: nasal bridge (extent indicated by dashed lines); p: posterior.

Fig. 8 Detail of surface models of (A) juvenile and (B) adult pike. Sagittal sections (locations indicated in Fig. 7) through nasal region (A: lateral part; B: medial part). Horizontal arrow: direction of free-stream flow. Vertical arrow indicates excurrent nostril normal to flow. Yellow outlines: nasal chamber. Dashed lines: rims of incurrent and excurrent nostrils. Light blue asterisked section: protruding dorsal edge of nasal bridge. Black marks, panel frames: position of transverse sections in Fig. 9. a: Anterior; d: dorsal; EN: excurrent nostril; IN: incurrent nostril; NB: nasal bridge; NF: nasal fold; NP: nasal passage; p: posterior; v: ventral.

Fig. 9 Detail of surface models of (A) juvenile and (B) adult pike. Transverse sections through nasal passage. Location of sections given in Figs. 7 and 8. Orientations same as Fig. A.5C, Appendix A.5 (juvenile pike) and Fig. 5C (adult pike). Asterisk: ventral surface of nasal bridge. Yellow disk: central posterior nasal fold. Green disk: sensory channel. NB: Nasal bridge; NP: nasal passage.

Fig. 10 Detail of surface models of (A) juvenile and (B) adult pike. Olfactory rosettes (dorsal sections through nasal region). Asterisk: central posterior nasal fold. Green disk: sensory channel. a: Anterior; EN and IN: location of excurrent and incurrent nostrils, respectively; l: lateral; m: medial; NF: nasal fold; p: posterior.

Fig. 11 Correspondence of CFD-generated streamlines to dye behaviour in the plastic models of the pike. The plastic models are represented by surface models. Streamline(s) (yellow tubes) correspond to dye behaviour in: (A) Video clip 1; (B) Video clip 2; (C) Video clip 5; (D) Video clip 7; (E) Video clip 9; (F) Video clip 10; (G) Video clip 11; and (H) Video clip 12 (video clip identified by number in box in each panel). (A) – (G): Adult pike; (H): juvenile pike. (A), (D) and (H): Lateral aspect of models. (B) and (C): Dorsal aspect. (E) and (F): Superior view (*left* nasal region in F). (G): Lateroventral aspect. Insets: magnified nasal region. Model in (C), (D) and (E) at 50 % opacity, to match translucent right nasal region of plastic model. Scale bars refer to the size of the *plastic* models. Arrow: direction of free-stream flow. Black lines: extent of nasal chamber. Red disk: nasal bridge. Blue disk: vortex. Asterisk: flow under eye. EN: Excurrent nostril (black on white lines); Ey: eye; IN: incurrent nostril (white lines); Lt and Me: lateral and medial routes through nasal chamber, respectively.

Fig. 12 CFD-generated streamlines (tubes) in the nasal region of the pike CFD models. (A) Flow deflected (1) dorsally and (2) ventrally by the nasal bridge. Adult pike, anterolateral aspect. Streamlines colour-coded according to speed (U). Asterisk indicates where dorsally directed flow meets ventrally directed flow. Circle: medial edge of nasal bridge. (B) Vortex (V1) in incurrent nostril. Juvenile pike, superior view. Inset: side view of V1 (indicated by eye in main panel), different streamline. Blue disks: points at which fluid particle in V1 is near olfactory sensory surface. (C) Vortex (V2) in excurrent nostril. Juvenile pike, superior view. Blue streamlines: flow passing through nasal chamber. Yellow streamlines: external flow. Blue asterisk: point at which external flow passes over excurrent nostril. For (B) and (C): model at 50 % opacity; black lines: limits of nasal chamber. Scale bar in (B) also applies to (C). (D) Persistence of incurrent vortex at different yaw angles. Adult pike, superior view. Yellow, red and blue streamlines: yaw 0°, + 5° and - 5°, respectively. Arrow: direction of free-stream flow. a: Anterior; EN: excurrent nostril; IN: incurrent nostril; l: lateral; m:

medial; NB: nasal bridge (extent indicated by dashed lines); NC: nasal chamber; p: posterior; V1: incurrent vortex; V2: excurrent vortex.

Fig. 13 Static pressure on the surface of (A) juvenile and (B) adult pike CFD models. Surfaces colour-coded according to pressure coefficient (*Cp*). Insets: anterior aspect of nasal region. Cross (insets) and arrow (main images): direction of free-stream flow (into page for cross). White lines, main images: division between $Cp > 0$ (predominantly red) and $Cp < 0$ (predominantly blue). Dashed black lines, insets: limits of nasal bridge. Dashed yellow line, inset in (A): midline of nasal bridge. White disk (main images): stagnation points. White disk (insets): region of maximum pressure in the nasal region (yaw $0 \pm 5°$). d: Dorsal; EN: excurrent nostril; Ey; eye; IN: incurrent nostril; l: lateral; m: medial; Ro: rostrum; v: ventral.

Fig. 14 CFD-generated streamlines passing through olfactory sensory channels of juvenile (A and B) and adult (C and D) pike CFD models. (A) and (C): Static pressure on nasal chamber floor. Surface colour-coded according to pressure coefficient (*Cp*). (B) and (D): Flow decelerating as it approaches nasal chamber floor. Streamlines colour-coded according to speed (*U*). White arrow: flow through sensory channel. Pair of yellow arrows: flow split by central posterior nasal fold (yellow asterisk). Black arrow: streamline exiting incurrent nostril. White disk: point of maximum *Cp* on nasal chamber floor. Green disk: sensory channel. Black asterisk: streamline passing *over* nasal fold. a: Anterior; EN and IN: location of excurrent and incurrent nostrils, respectively; l: lateral; m: medial; NF: nasal fold; p: posterior.

Fig. 15 Incurrent nostril entry points for CFD-generated streamlines passing through the olfactory sensory channels in the nasal chamber of (A) juvenile and (B) adult pike CFD models. Slice (grey) through CFD mesh of right incurrent nostril. Numbered black lines: speed contours normalised to maximum flow speed in slice (4.7 cm s^{-1}). 1: 0.2; 2: 0.4; 3: 0.6; 4: 0.8. White region: area through which 'sensory channel' streamlines pass. a: Anterior; l: lateral; m: medial; p: posterior.

Fig. 16 Boundary layers (blue) in the pike CFD models. (A) and (C): Lateral aspect of head of juvenile and adult pike, respectively. Yellow regions: space occupied by streamlines (Appendix A.1.7.5). *t*: time taken for a fluid particle to get from the point of entry into the

boundary layer to the incurrent nostril. Insets: dorsal aspect of rostral tip (right section), showing where streamlines enter boundary layer. (B) and (D): Sagittal sections (indicated in Fig. 7) of nasal region of juvenile and adult pike, respectively. Dashed black line: outer limit of boundary layer of mutant model (Section 2.4). Dashed white line: outline of head of mutant model. Asterisk: bulge in boundary layer. Curved line: lower limit of round inset. Round inset in (B) and (D): magnified dorsal edge of nasal bridge. White lines in round inset: speed contours (normalised to maximum flow speed in corresponding slice through CFD mesh). Rectangular inset in (B): key parts of nasal region. Arrow: direction of free-stream flow. a: Anterior; BL: boundary layer; d: dorsal; EN: excurrent nostril; Ey: eye; IN: incurrent nostril; NB: nasal bridge; p: posterior; v: ventral.

Fig. 17 Schematic of flow in the nasal region of the pike. Main image: sagittal section through nasal region of adult pike (location of section indicated in Fig. 7B). Inset: sagittal section through excurrent nostril of juvenile pike. Large white arrow: direction of free-stream flow. Red arrow: flow deflected dorsally and ventrally by nasal bridge. Blue arrows: vortices. Yellow arrows: central nasal passage flow. Small white arrow: sensory channel flow. Arrows 1 – 4: viscous forces. Red disk: flow deflected dorsally and ventrally by nasal bridge. White disk: flow dispersed on nasal chamber floor. Dashed yellow circle: entrained fluid. a: Anterior; d: dorsal; EN: excurrent nostril; IN: rim of incurrent nostril; NB: nasal bridge; p: posterior; v: ventral; V1: incurrent vortex; V2: excurrent vortex.

Video

Dye visualisation with the plastic models of the pike. Flow is left to right and the free-stream speed is 5 cm s^{-1}. Pitch and yaw are 0°. Roll angles and camera positions (Fig. A.3, Appendix A.5) are given below. Unless stated otherwise: the right nasal region is shown; the dorsal aspect camera position (Fig. A.3B, Appendix A.5) is X; and each clip is flipped horizontally.

Clip 1 Adult pike. Passage of dye over rostrum and through nasal chamber. Lateral aspect of head. Roll 0°; camera position a. Compare with Fig. 11A.

Clip 2 Adult pike. Passage of dye over rostrum and through nasal chamber. Dorsal aspect of head. Roll + 90°; camera position b. Clip rotated 180°. Compare with Fig. 11B.

Clip 3 Adult pike. Passage of dye through *left* nasal chamber. Dorsal aspect. Roll + 90°; camera position a. Compare with Fig. A.8A, Appendix A.5.

Clip 4 Juvenile pike. Passage of dye through nasal chamber. Lateral aspect. Roll 0°; camera positions a and Y. Compare with Fig. A.8B, Appendix A.5.

Clip 5 Adult pike. Passage of dye through nasal chamber. Dorsal aspect. Roll + 90°; camera position b. Clip rotated 180°. Compare with Fig. 11C.

Clip 6 Juvenile pike. Dye takes two routes through nasal chamber. Superior view of nasal region. Roll + 45°; camera positions a and Y. Clip rotated 180°. Compare with Fig. A.8C, Appendix A.5.

Clip 7 Adult pike. Dye takes two routes through nasal chamber. Lateral aspect. Roll 0°; camera position a. Compare with Fig. 11D.

Clip 8 Juvenile pike. Vortex in incurrent nostril. Superior view of nasal region. Roll + 45°; camera positions a and Y. Clip rotated 180°. Compare with Fig. A.8D, Appendix A.5.

Clip 9 Adult pike. Vortex in incurrent nostril. Superior view of nasal region. Roll + 45°; camera position a. Clip rotated 180°. Compare with Fig. 11E.

Clip 10 Adult pike. Probable passage of dye through posterior sensory channels. Superior view of *left* nasal region. Roll + 150°; camera position a. Compare with Fig. 11F.

Clip 11 Adult pike. Passage of dye over nasal bridge. Lateroventral aspect. Roll - 60°; camera position a. Compare with Fig. 11G.

Clip 12 Juvenile pike. Passage of dye over excurrent nostril. Lateral aspect. Roll 0°; camera position a. Compare with Fig. 11H.

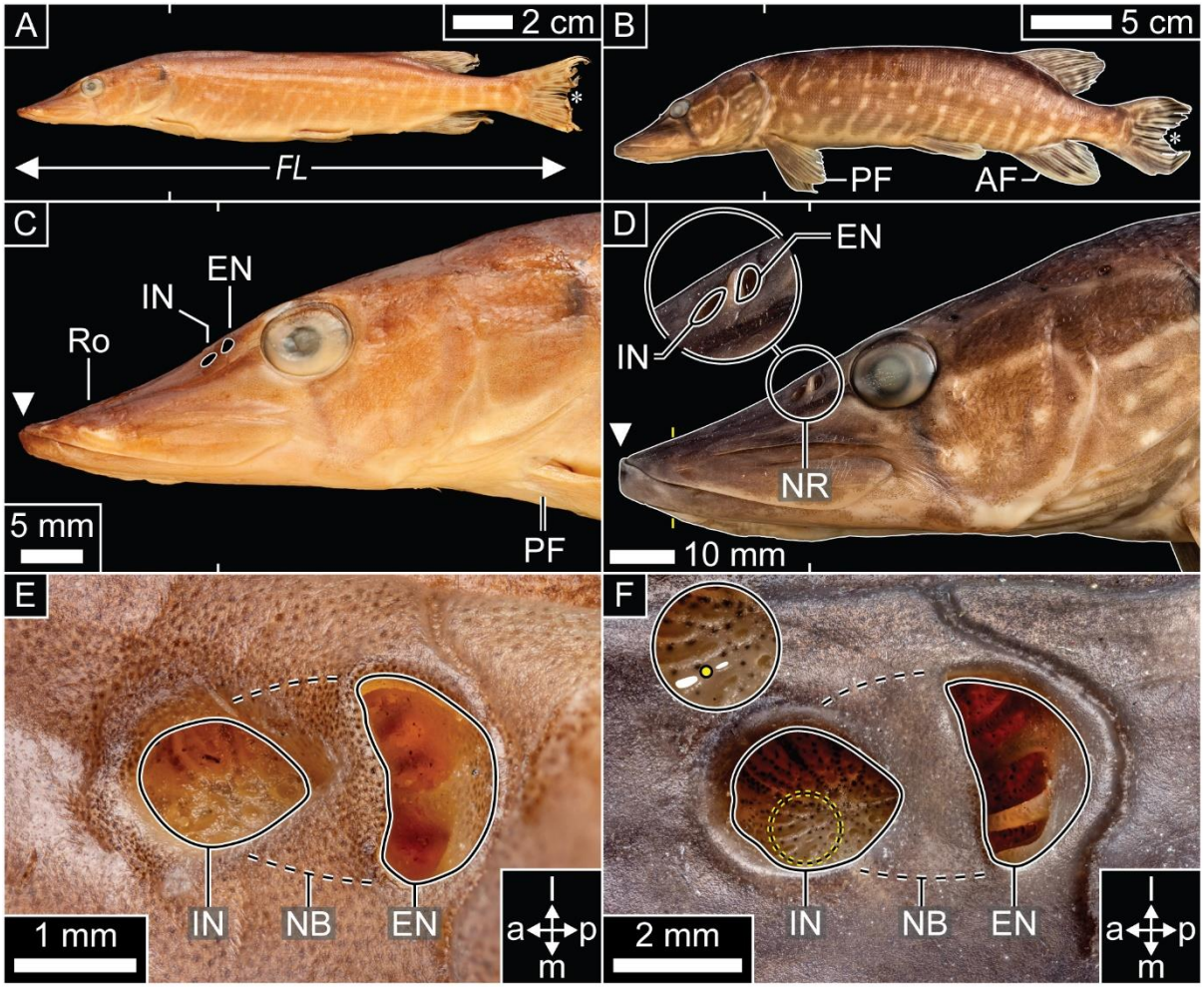

Fig. 1 The two pike (*Esox lucius*) specimens used to generate the fluid dynamics models.

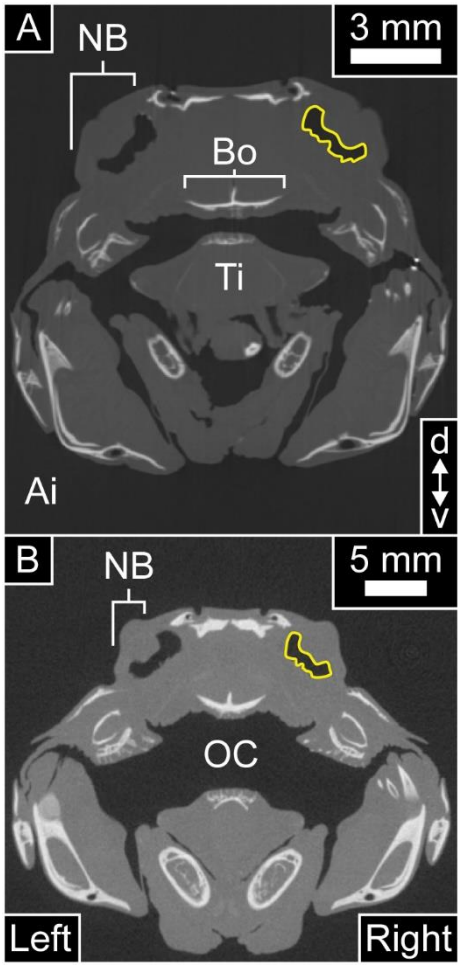

Fig. 2 TIFF images from micro-CT scans of (A) juvenile and (B) adult pike.

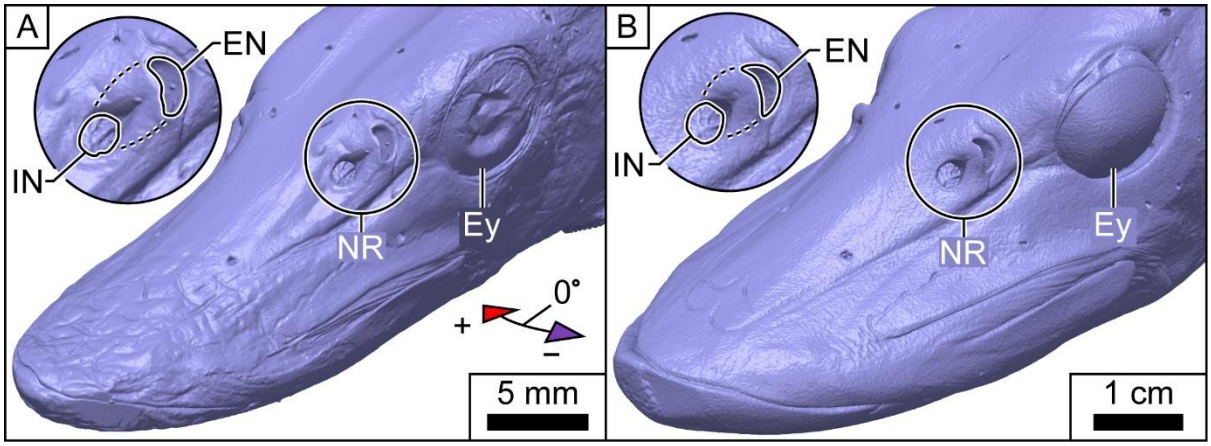

Fig. 3 Surface models of heads of (A) juvenile and (B) adult pike.

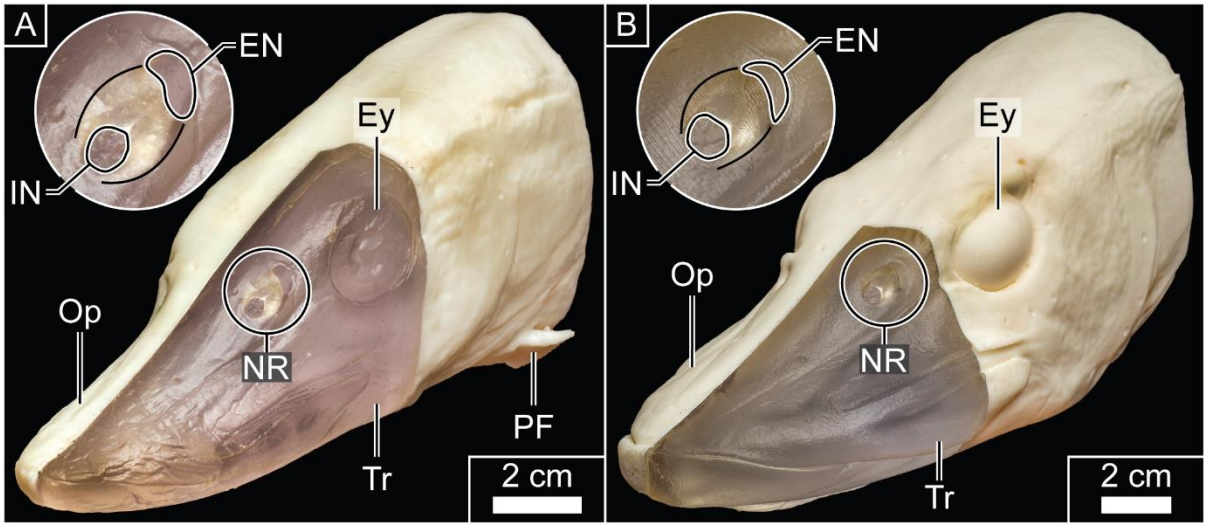

Fig. 4 Plastic models of heads of (A) juvenile and (B) adult pike.

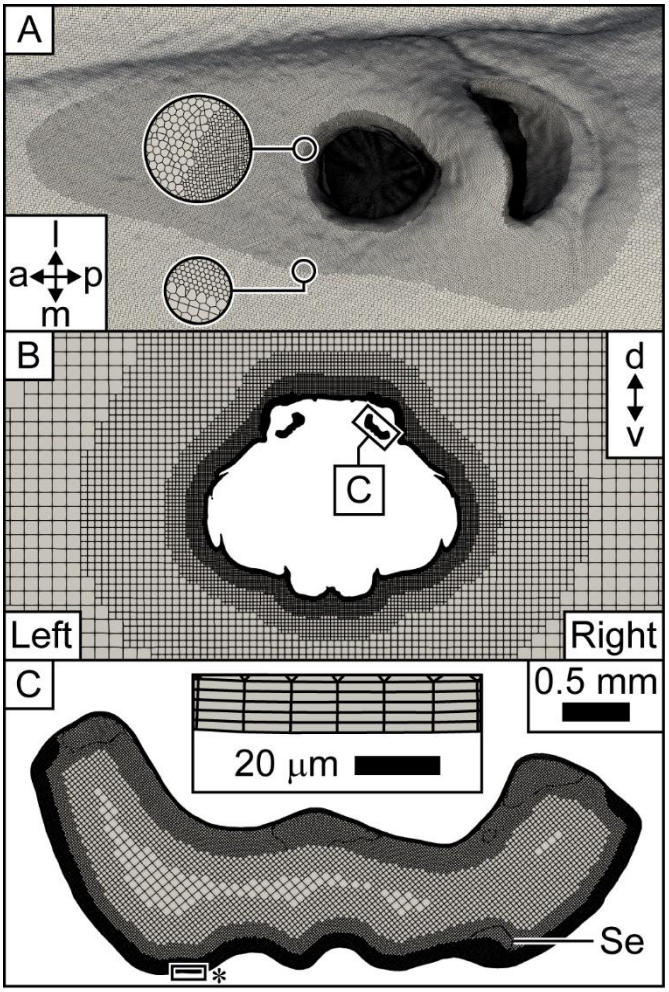

Fig. 5 CFD mesh of adult pike.

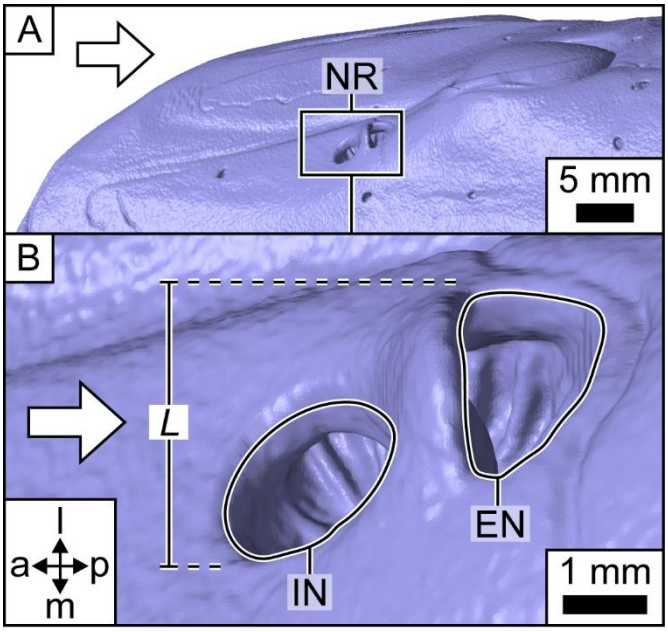

Fig. 6 Characteristic dimension of adult pike's nasal region.

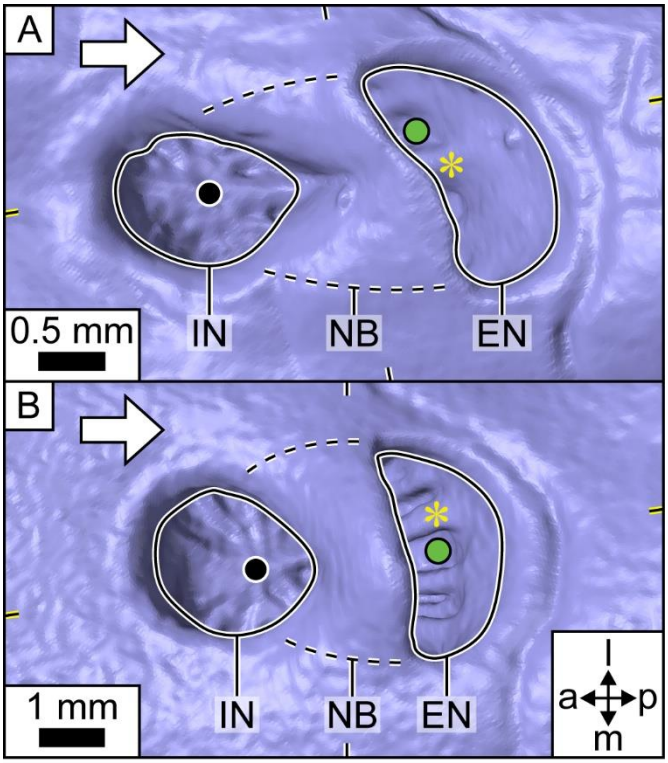

Fig. 7 Detail of surface models of (A) juvenile and (B) adult pike.

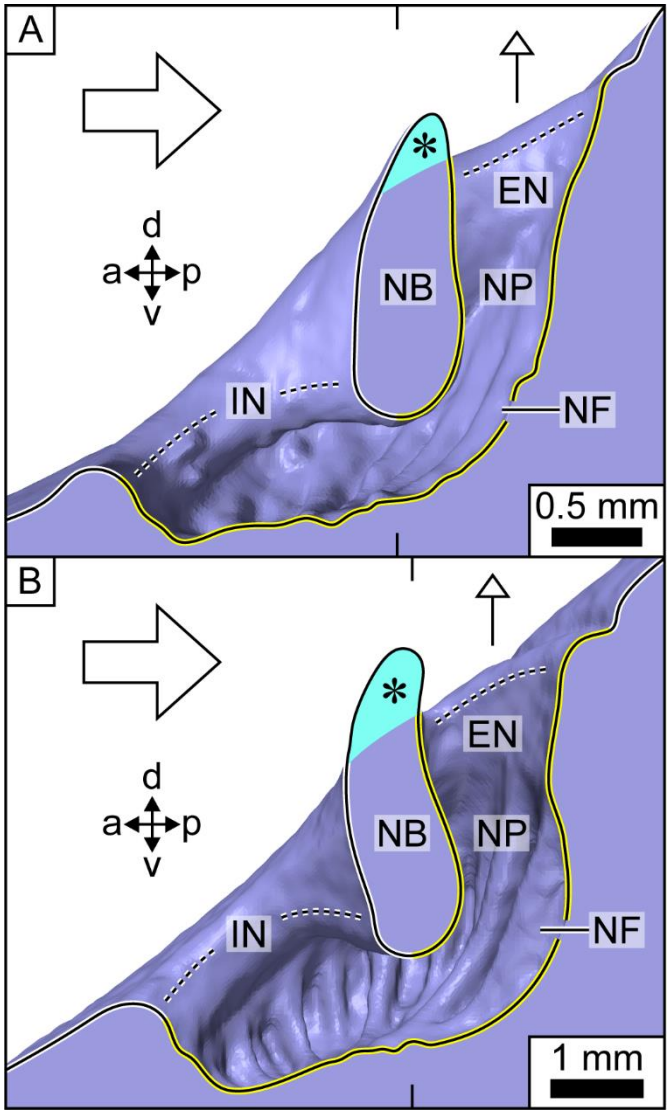

Fig. 8 Detail of surface models of (A) juvenile and (B) adult pike.

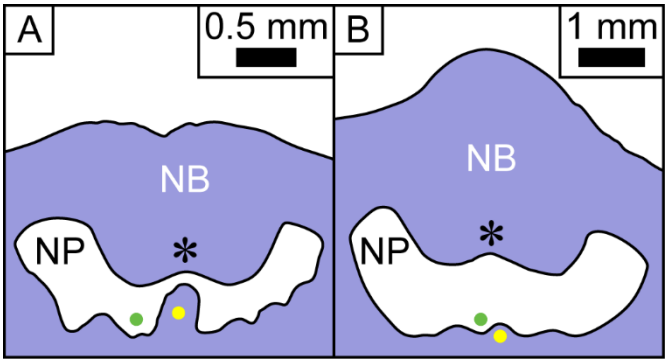

Fig. 9 Detail of surface models of (A) juvenile and (B) adult pike.

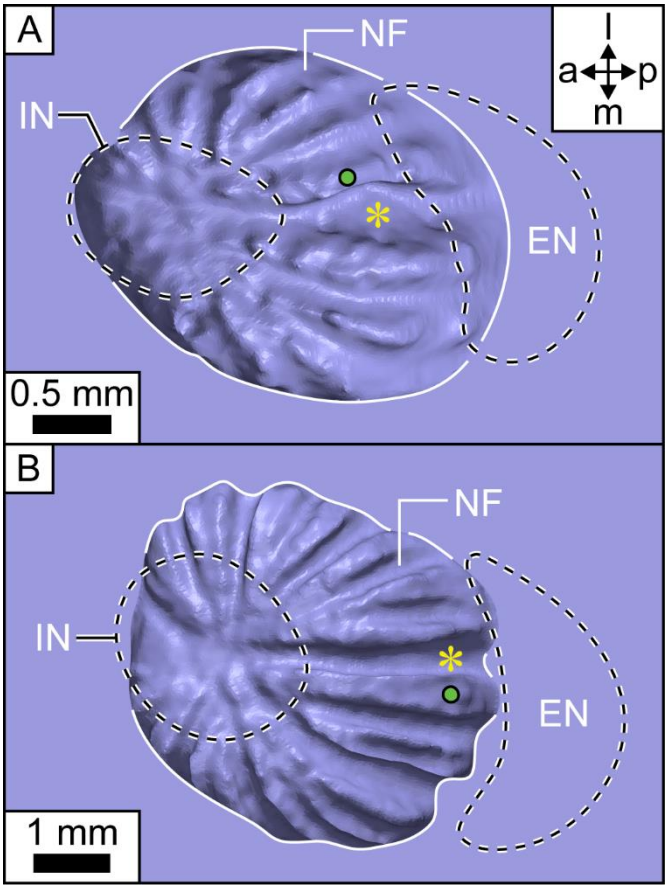

Fig. 10 Detail of surface models of (A) juvenile and (B) adult pike.

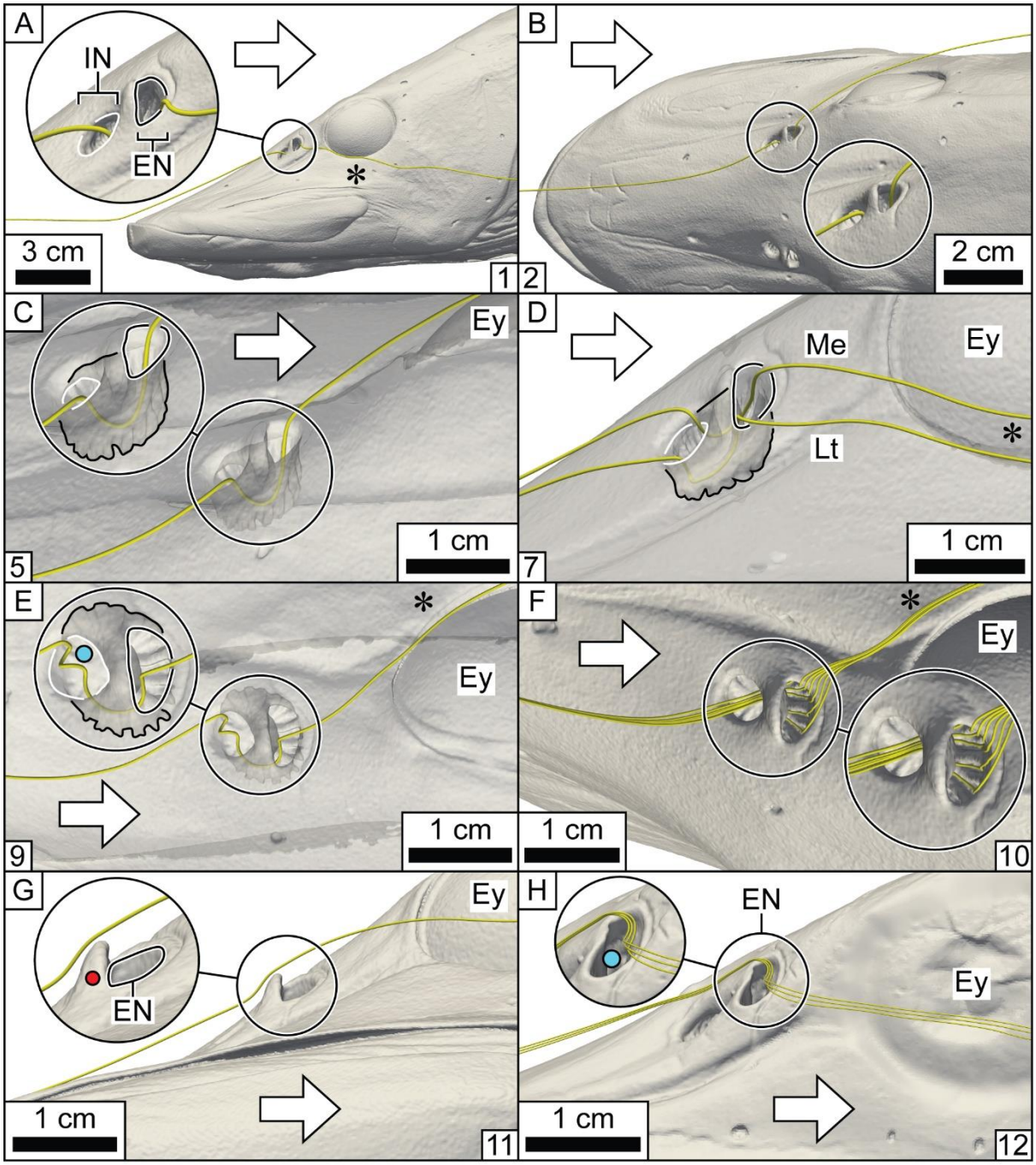

Fig. 11 Correspondence of CFD-generated streamlines to dye behaviour in the plastic models of the pike.

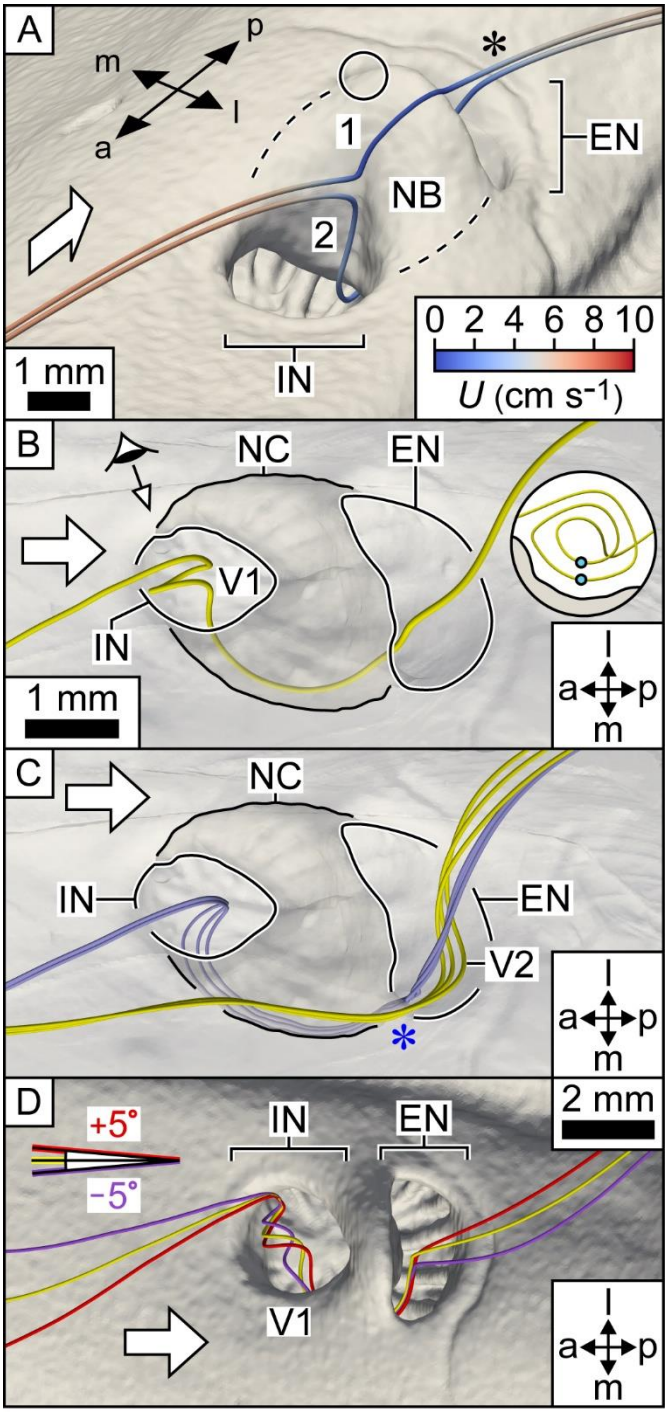

Fig. 12 CFD-generated streamlines (tubes) in the nasal region of the pike CFD models.

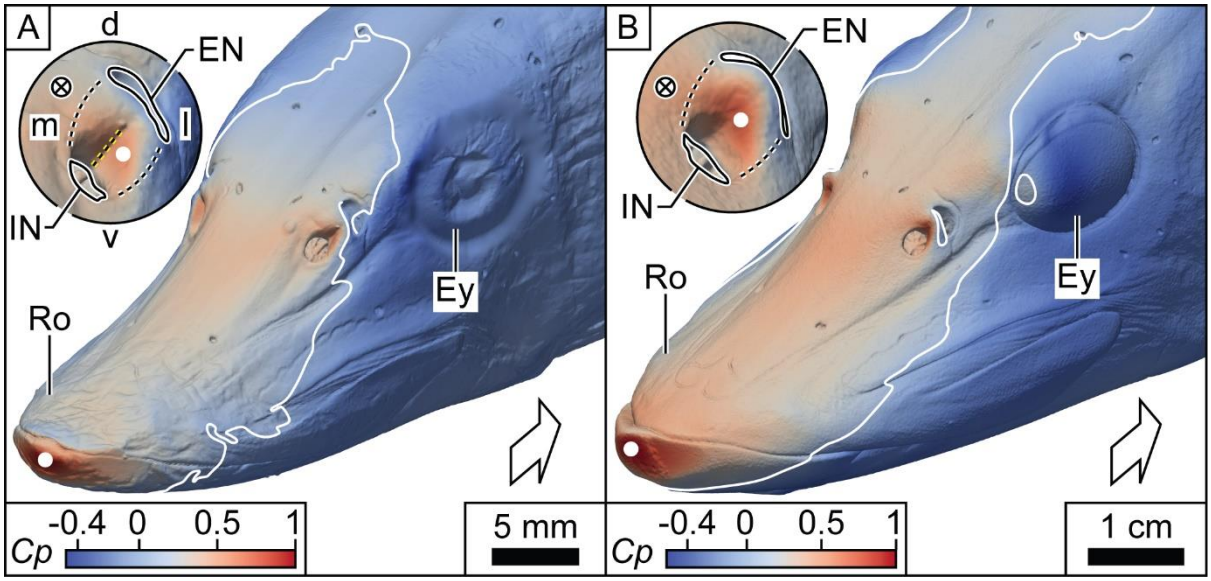

Fig. 13 Static pressure on the surface of (A) juvenile and (B) adult pike CFD models.

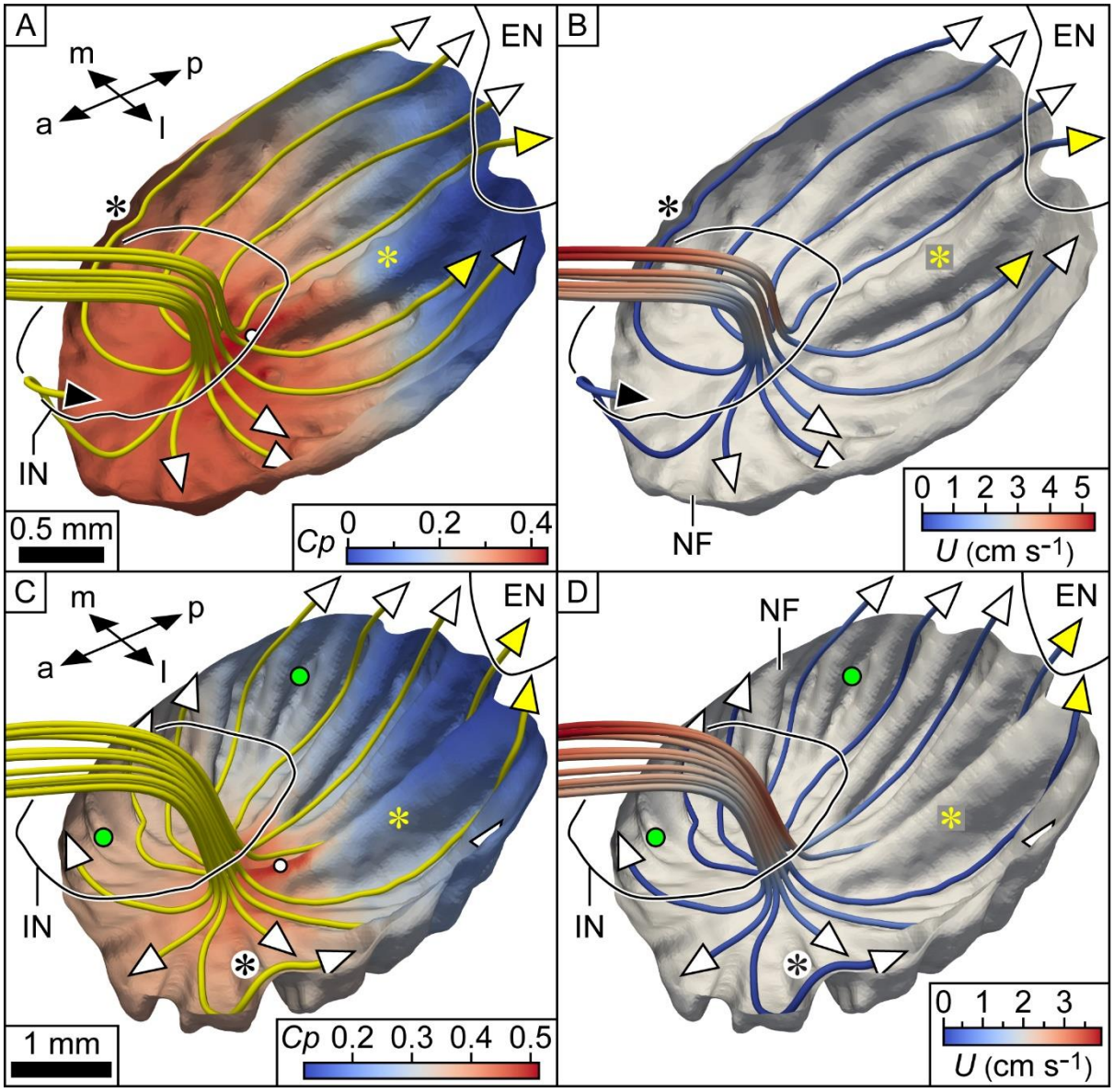

Fig. 14 CFD-generated streamlines passing through olfactory sensory channels of juvenile (A and B) and adult (C and D) pike CFD models.

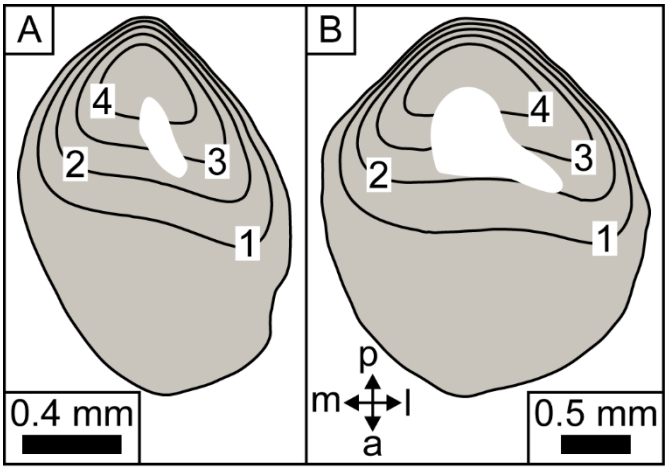

Fig. 15 Incurrent nostril entry points for CFD-generated streamlines passing through the olfactory sensory channels in the nasal chamber of (A) juvenile and (B) adult pike CFD models.

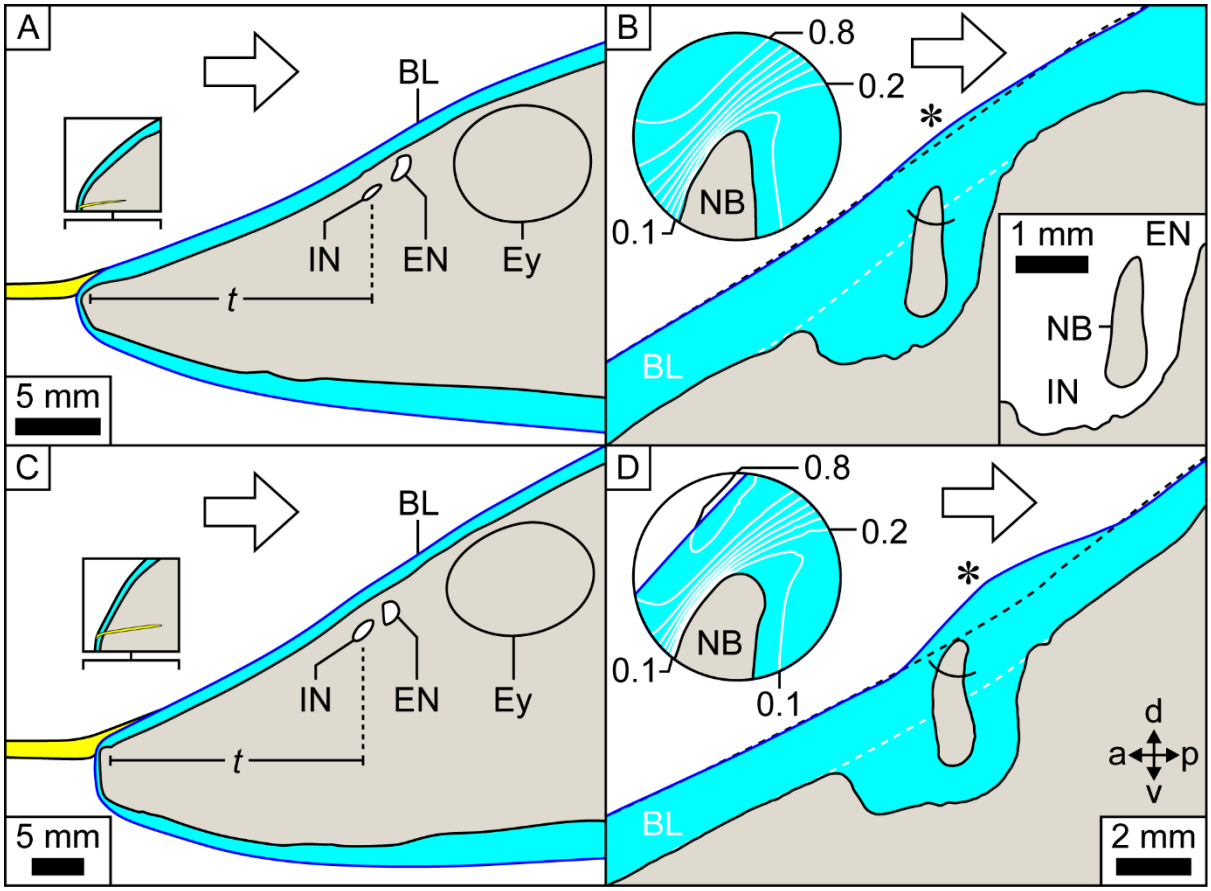

Fig. 16 Boundary layers (blue) in the pike CFD models.

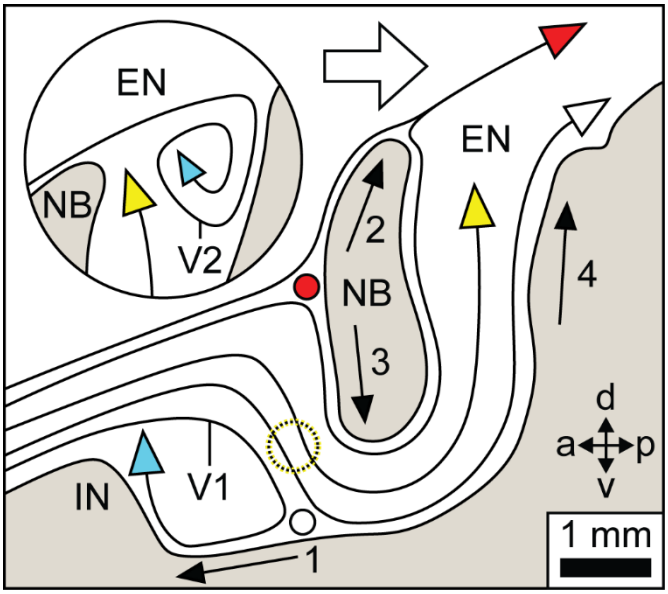

Fig. 17 Schematic of flow in the nasal region of the pike.

Specimen	Free-stream speed (cm s^{-1})	Model	Total drag of model (mN)	Percentage contribution of nasal region to total drag[c]	Percentage contributions of pressure drag (P) and viscous drag (τ) to entire model or nasal region			
					Entire model		Nasal region[c]	
					P	τ	P	τ
Juvenile	15	Wild type[a]	1.32	5.4	14	86	77	23
		Mutant[b]	1.32	5.3	14	86	77	23
Adult	10	Wild type	2.88	4.0	24	76	86	14
		Mutant	2.87	3.6	23	77	88	12

Table 1 Drag forces and contributions to drag in the CFD models of juvenile and adult pike. a) Wild type: model with unaltered nasal region. b) Mutant: model in which the nostrils and nasal chamber of each nasal region have been replaced by a continuous surface that blends smoothly with the rest of the head. c) Values given are for the two *combined* nasal regions. Highlighted entries are referred to specifically in the main text.

Appendix A

A.1. Additional methodology

A.1.1. X-ray micro-computed tomography

For the X-ray micro-computed tomography (micro-CT) scan of the juvenile pike, the specimen was held in a truncated 500 cm^3 plastic measuring cylinder (height 14 cm; inner diameter 4.8 cm), with the body axis vertical and the head uppermost. To prevent the specimen undergoing unwanted movements during the scan, it was wrapped in plastic film, covering the body (but not the head) to the base of the pectoral fins, and then packed tightly against the side of the cylinder with bubble-wrap, leaving the head protruding from the top of the cylinder. Subsequently, to prevent the specimen drying out during the scan, several drops of preservative fluid (70 % industrial methylated spirits, 30 % distilled water) were put on the head and a plastic sleeve was placed over the entire arrangement. The X-ray beam was generated from a rotating tungsten reflection target. Exposure time (single image), accelerating voltage, and current were 708 ms, 90 kV, and 332 μA, respectively. A total of 2799 projections were collected in a single 360° rotation at 0.128617° intervals. The scan of the juvenile pike was also used to generate the nasal region and nasal volume models (Appendix A.2).

For the micro-CT scan of the adult pike, the specimen was held in a 1000 cm^3 plastic measuring cylinder (height 26.5 cm; inner diameter 7.7 cm), with the body axis vertical and the head uppermost. To prevent the specimen undergoing unwanted movements during the scan, it was placed in a plastic sleeve and a strip of muslin wrapped around the *outside* of the sleeve, in the pectoral fin region (Fig. 1, PF), lodging the specimen firmly in place. (Placing the muslin inside the sleeve would have resulted in it absorbing preservative fluid from the specimen, causing the latter to shrink and therefore move during the scan.) To prevent the specimen drying out during the scan, 100 cm^3 of preservative fluid was added to the plastic sleeve, such that the level of fluid was just below the posterior edge of the anal fins (Fig. 1B, AF). A plastic sleeve was placed over the head (without touching it) for the same purpose. We left the specimen in this arrangement for 4 hours before performing the scan, to allow excess preservative fluid to drain from the nasal chamber. (Excess preservative fluid, particularly between the nasal folds [e.g. Fig. 14D], would have blurred the surface of the

specimen in the resultant scan, because pixels corresponding to preservative fluid have similar intensities to pixels corresponding to tissue stored in preservative fluid.) The X-ray beam was generated from a static tungsten reflection target and passed through a 0.5 mm copper filter. Exposure time (single image), accelerating voltage, and current were 708 ms, 170 kV, and 70 μA, respectively. A total of 3142 projections were collected in a single 360° rotation at 0.114577° intervals.

A second, higher resolution, micro-CT scan of the adult pike was used to generate the (right) nasal region and nasal volume models (Appendix A.2). The mounting conditions and X-ray parameters for the second scan were the same as the first. The second scan comprised 1747 TIFF images and had a voxel size of 32.5 μm x 32.5 μm x 32.5 μm ([dataset] Garwood et al., 2020b).

Projections from the three scans were transformed into a three-dimensional matrix using CT-Pro (Nikon Metrology, Tring, UK). The scans were converted into 8-bit TIFF images using VGStudio MAX (Version 2.2, Volume Graphics GmbH, Heidelberg, Germany) for the juvenile pike and Drishti (Version 2.6.3; Limaye, 2012) for the adult pike.

A.1.2. Surface models

Surface models of the heads of the pike specimens were created as follows. TIFF images from each micro-CT scan were imported into ScanIP and segmented with the Threshold tool, creating a 'mask' of the complete head ('head' mask). For thresholding, we chose a lower value of either 53 (juvenile pike) or 55 (adult pike) and an upper value of 255. These values were chosen because they gave masks with smooth surfaces whilst preserving the anatomical detail of the nasal regions. Internal cavities (e.g. the oral cavity [Fig. 2B, OC] and the lateral line canals [Fig. A.1A, filled yellow regions; Fig. 6.2A of Helfman et al., 2009]) were filled using the Floodfill and Paint tools. (The internal cavities were filled to reduce the size of the stereolithography [STL] file prior to 3D printing/conversion to the computational fluid dynamics mesh.) The head mask was adjusted to either a) life size, b) 3x life size (juvenile pike), or c) 2x (adult pike) life size with the Rescale tool.

We performed additional image processing on the head mask of the adult pike. First, the head mask was smoothed with a Recursive Gaussian filter (sigma x, y and z values: one pixel, for

the same reason that we chose the thresholding values). Next, a relatively small protrusion on the dorsal surface of the head mask was removed using the Paint tool . Based on a region of intense pixels at this point in the micro-CT scan (Fig. A.1C, circle), together with a visual inspection of the specimen, we surmise that the protrusion was caused by a fragment of metal or glass. The amended surface, together with a micro-CT artifact on the rostral tip, was then smoothed using the 3D editing tool (Cylinder for amended surface, Cuboid for rostral tip) (Fig. A.1D, circle, and Fig. A.2). The artifact on the rostral tip probably arose from at that point a combination of noise and poor contrast between the air and the specimen.

Two new masks were created from the larger-than-life head masks of the juvenile and adult pike: an 'opaque' mask corresponding to each plastic model's opaque part (Fig. 4, Op); and a 'translucent' mask corresponding to the translucent part (Fig. 4, Tr). The translucent mask was isolated from the head mask with the Floodfill tool. The opaque mask was generated with the Boolean operations tool by subtracting the translucent mask from the head mask. The Paint tool was used to put a hole in the back of the opaque mask (for the plastic model's aluminium peg, Fig. A.3A, Pe). To generate an STL model of manageable size for 3D printing, the pixel spacing of the opaque mask of the juvenile pike was adjusted to 59 μm with the Resample tool. The opaque mask of the adult pike was not, however, resampled. A surface model was created from each of the three types of mask (head, opaque, translucent) with the following features (de)selected in ScanIP's 'Model configuration' dialogue box: a) 'General' tab → Smart mask smoothing (pre-processing) → Use greyscale values; b) 'Surface settings' tab → Triangle smoothing → Use triangle smoothing for masks (10 iterations); and c) 'Surface settings' tab → Decimation → Decimate box: 10 % for opaque and translucent masks of juvenile pike, unticked for all other masks. The surface models were then each exported in binary format as STL files.

STL files of the nasal regions and nasal volumes (a nasal volume being the space occupied by water in the nasal chamber) were created using the same methodology as above (see also Appendix A.1.5 of Garwood et al., 2019).

A.1.3. Plastic models

The two parts of each plastic model of the pike's head were 3D printed from the corresponding STL files according to the methodology of Abel et al. (2010). The opaque part

(Fig. 4, Op) of each model was made in off-white plastic (ABS for the juvenile pike, ASA for the adult pike; both Stratasys, Eden Prairie, USA), to give good contrast with the red dye used to visualise flow. The translucent part of each model, which included the right nasal region (Fig. 4, Tr), was made in VisiJet SL Clear plastic (3D Systems, Rock Hill, South Carolina, USA), to facilitate dye visualisation within the nasal chamber. For both models we chose the right nasal region for the translucent part, either because its excurrent nostril was better defined than that of the left nasal region (juvenile pike) or because its nasal folds were more pronounced than those in the left nasal region (adult pike). The thickness of the layers arising from the 3D printing process was either 178 μm (opaque part) or 50 μm (translucent part). The appropriate opaque part and translucent part were glued together to give a complete model (Fig. 4). An aluminium peg (Fig. A.3A, Pe; see also Fig. 4 of Garwood et al., 2019) was inserted into the back of each model, allowing the model to be fixed to the rig used to suspend it in the flume.

Plastic models of the nasal regions and nasal volumes were 3D printed using the above methodology. Each plastic model of a nasal region comprised two parts: the nasal region minus the nasal bridge, and the nasal bridge. The plastic model of the nasal bridge fitted into the plastic model of the nasal region to give a model of the complete nasal region. The ability to remove the nasal bridge from the complete model helped determine the detailed arrangement of nasal folds (Appendix A.2). The plastic models of the nasal regions/volumes were 12.5x (juvenile pike) and 5x (adult pike) life size, and were made in off-white plastic (ASA).

A.1.4. Environmental currents likely to be encountered by a stationary pike

The current in either a lake, or a slow-flowing stream, or a river, all typical freshwater habitats of a pike (Chapman and Mackay, 1984; Masters et al., 2002), is ≤ 30 cm s^{-1} (Horne and Goldman, 1994, p. 72; James et al., 2005, p. 108; Macan, 1974, p. 32).

A.1.5. Cruising speed of a pike

The pike that we observed at the Aquarium of the Lakes cruised (Webb, 1984) at speeds in the range 8 – 24 cm s^{-1} (average = 15 cm s^{-1}, n = 11), corresponding to 0.08 – 0.3 *FL* s^{-1} (*FL* = 75 – 100 cm; Section 2.2). Webb (1984) gives a range of cruising speeds for the pike of 1 – 4 body lengths s^{-1}. Assuming body length is total length (Fig. 2.2 of Helfman et al., 2009), and

given that in the pike total length is essentially fork length (Fig. 1A), these data give a range of cruising speeds of 0.08 – 4 *FL* s^{-1}.

A.1.6. Dye visualisation

The working section (L x W x H) of the Eidetics Model 1520 flume was 152 cm x 38 cm x 51 cm. Each model was suspended in the flume via its aluminium peg using the rig described in Abel et al. (2010). The rig/peg arrangement also allowed the roll (Fig. 10.1 of Barnard and Philpott, 2004) of the model to be varied (Fig. A.3A, Rl). The model was positioned such that it was central (± 2 cm) width-wise to the working section of the flume. The maximum transverse cross-sectional area of each model was 36 cm^2 (juvenile pike) and 64 cm^2 (adult pike), both less than 5 % of the working cross-sectional area of the flume. The effect from the walls of the flume on flow in the vicinity of the model should therefore have been negligible, based on standard corrections (Barlow et al., 1999, p. 361). The model of the juvenile pike was illuminated with a quartz lamp fitted with a white screen to diffuse light; that of the adult pike was illuminated with a halogen lamp. White card was placed behind each model to help visualise dye. The dye solution was introduced from a pressurised reservoir using stainless steel tubing (internal diameter 1.3 mm; external diameter 2 mm). The horizontal section of this tubing, from which dye was released, was 27 cm (juvenile pike) or 25 cm (adult pike) from the flume's floor. At a free-stream speed of 5 cm s^{-1}, dye emerged from the tubing as a well-defined filament, indicating that the exit velocity of the dye was equal to the local flow velocity (Fig. 3.1 of Lim, 2000). To minimise the effect of the tubing on flow over the models (Lim, 2000), the aperture of the tubing was located some distance (juvenile pike: 5 cm; adult pike: 12 – 16 cm) upstream from the point of impingement on the model. The dye, as a filament, was directed at the anterior rostral edge of each model (Video clip 1).

A.1.7. Computational fluid dynamics

A.1.7.1. Simulations

Each mesh for a computational fluid dynamics (CFD) simulation was derived from the STL model of the respective head (Appendix A.1.2). Before converting the STL models to CFD meshes, we modified them in several ways. First, we added a tapered extension ('tail') to the back of each STL model (Fig. A.4, Ta). The tails were approximately 4x (juvenile pike) or 5x (adult pike) the length of the head; each had a 7° taper (Fig. A.4). We added each tail to

prevent flow separating from the back of the head, and to reduce therefore any modification to upstream flow due to the lack of a body (Garwood et al., 2019). Second, we smoothed the rim of each eye, in order to avoid the formation of small pockets within the subsequent mesh. Such pockets may have caused the simulations to stop prematurely. Finally, in the model of the juvenile pike, we removed the base of each pectoral fin (Appendix A.3). We made the modifications using GeoMagic Wrap (3D Systems; Appendix A.1.4.2 of Garwood et al. 2019). Each STL model was converted to a CFD mesh with the snappyHexMesh utility of the software OpenFOAM (Weller et al., 1998). The computational domains for the simulations had a velocity inlet and a pressure outlet. The dimensions (L x W x H) of the computational domains were 10.9 m x 2.1 m x 2.1 m (juvenile pike), and 30.0 m x 5.6 m x 5.6 m (adult pike). Each model lay at the centre of the domain in the transverse plane. The rostral tips were positioned 4.3 m (juvenile pike) or 11.9 m (adult pike) from the velocity inlet. The size of the computational domain, together with the position of the model within it, were chosen to minimise flow artifacts from the walls of the domain. The no-slip condition was set for all solid surfaces, together with a symmetry plane (with a zero gradient of velocity and pressure across the plane) at the dorsal, ventral, and lateral surfaces of the domain. The Navier-Stokes equations governing transient laminar flow were solved with the OpenFOAM algorithm PIMPLE. The Navier-Stokes equations governing steady laminar flow were solved with the OpenFOAM algorithms SIMPLE (juvenile pike) and SIMPLEC (adult pike), respectively. Solutions to the Navier-Stokes equations gave a field of velocity vectors.

The terms UMean, pMean, and tauMean in Appendices A.1.7.3, A.1.7.5 and A.1.7.6 are the average velocities, static pressure, and shear stress over the last 500 iterations of the converged, time-averaged solution to the Navier-Stokes equations for a given simulation. The units of pMean and tauMean when generated by the simulation are energy per unit mass. Therefore, to convert pMean and tauMean to the units of pressure (pascals), both must be multiplied by the density of water.

A.1.7.2. Pressure

Points of relatively high static pressure on the surface of a CFD model were located using ParaView's Find Data tool.

The average static pressure in each nostril ($P - P_0$ in Equation 1 of the main text) was calculated in ParaView by using the Slice filter to put through the mesh a plane that passed

through the nostril, and then applying to that plane the following succession of filters: Connectivity → Threshold (to isolate the segment of the plane in the nostril) → Calculator (to calculate the static pressures at all points within this segment) → Integrate Variables. The average static pressure in the segment was then found by dividing the 'pressure' entry (Attribute: Point Data) in the Spreadsheet view by the Area entry (Attribute: Cell Data).

Note that Equation 2 (main text) is a more rigorous way of expressing the pressure difference across the nostrils than the one we used in our work on the sturgeon, *Huso dauricus* (Garwood et al., 2019). In the latter, for *Cp*(Incurrent nostril) we used the maximum static pressure in the nasal region (located on the lateral wall of the incurrent nostril of *H. dauricus*; Fig. 11B of Garwood et al., 2019). Ideally, the pressure difference across the nostrils should be calculated using the incurrent and excurrent faces of a control volume (Massey, 1989, p. 115), here the incurrent and excurrent faces of the nasal volume. Using Equation 2, we recalculated *ΔCp* for *H. dauricus*, in order to compare it with *ΔCp* for the juvenile and adult pike.

A.1.7.3. Streamlines

Streamlines were generated in ParaView by first applying the Stream Tracer With Custom Source filter to a point, with the following menu selections (selections in brackets): Vectors (UMean); Interpolator Type (Interpolator with Point Locator); Integration Direction (Both); Integrator Type (Runge-Kutta 4.5); Integration Step Unit (Cell Length); Initial Step Length (0.2 m); Minimum Step Length (0.01 m); Maximum Step Length (0.5 m); Maximum Steps (2000); Maximum Streamline Length (0.2 m); Terminal Speed (10^{-12} m s^{-1}); Maximum Error (10^{-6}). The Tube filter was then applied to the Stream Tracer With Custom Source filter, with the following menu selections (selections in brackets): Scalars (Angular Velocity); Vectors (Normals); Number of Sides (6); Radius (juvenile pike: typically 2 x 10^{-5} m; adult pike: typically 3.5 x 10^{-5} m). Points were created from the Sources menu (Point Source).

A.1.7.4. 'Mutant' models

Mutant models (Fig. A.7B and D; Section 2.4) were generated with GeoMagic Wrap (3D Systems), as follows. First, the polygons bounding each nasal region were selected with the Paint Brush Selection tool (Select Visible button active) and then removed (Polygons → Delete command). Next, the isolated nasal region was deleted (Paint Brush Selection tool →

select a group of polygons within the isolated nasal region → Bounded Components → Delete). Finally, the nasal region was replaced with a continuous surface (Polygons → Fill Holes → Fill Single → Complete → Curvature, with the nasal region boundary selected). The resultant surface mimicked the curvature of the head in the nasal region.

A.1.7.5. Boundary layer

The vorticity contour used to gauge the thickness of the boundary layer on the surface of a model was generated in ParaView by applying the following succession of filters to the fluids file (selections in brackets): Compute Derivatives (Vectors: UMean; Output Vector Type: Vorticity; Output Tensor Type: Vector Gradient); Cell Data to Point Data; Calculator (Result Array Name: Vorticity; subsequent box entry: mag(Vorticity)); Slice (optional); Contour (Contour by: Vorticity; Value Range: 5 [i.e. 5 s^{-1}]).

The boundary layers in Fig. 16A and C were created by superimposing the head on the three-dimensional boundary layer generated by the method above. Each yellow region in Fig. 16A and C is the space occupied by 10 streamlines generated from a line of 10 regularly spaced points across (in the transverse sense) the right incurrent nostril. The radius of each streamline was 2 x 10^{-5} m (juvenile pike) or 5 x 10^{-5} m (adult pike).

The time taken (*t*, Fig. 16A and C) for a fluid particle to get from the point of entry into the boundary layer to the incurrent nostril was estimated as follows. First, from the Sources menu (Point Source), we put 10 uniformly scattered points in the mesh plane through the incurrent nostril (Appendix A.1.7.2). From each point we then created a streamline (Appendix A.1.7.3; Integration Direction: Backward). Using the Hover Points On function, we then identified the point at which the streamline entered the boundary layer, and read the integration time from the Spreadsheet view.

A.1.7.6. Drag

Pressure drag and viscous drag were estimated in ParaView by applying the following series of filters to the surfaces.case file of a CFD model, or a segment of this model (isolated from the surfaces.case file with the Extract Block filter): 1) Extract Surface; 2) Generate Surface Normals; 3) Calculator (Result Array Name: Pressure; subsequent box entry: density*pMean); 4) Calculator (Result Array Name: Pressure Normals; subsequent box entry:

Pressure*Normals); 5) Calculator (Result Array Name: Shear Stress; subsequent box entry: density*tauMean); 6) Surface Vectors (Select Input Vectors: Shear Stress; Constraint Mode: Parallel); 7) Integrate Variables. Pressure drag was the first entry in the row of three values under the heading 'Pressure Normals' in the Spreadsheet view (i.e. pressure drag in the *x*-direction); viscous drag was the first entry in the row of three values under the heading 'Shear Stress' in the Spreadsheet view (i.e. viscous drag in the *x*-direction).

A.2. Detailed arrangement of nasal folds in the olfactory rosette

To compare the detailed arrangement of nasal folds in the right olfactory rosette of the juvenile and adult pike with the description given by Holl (1965), we used larger-than-life plastic models of both a) the nasal region and b) the nasal volume (Fig. A.10; Appendix A.1.3). We counted 12 folds in the juvenile pike (Fig. A.10A). We were unable, however, to distinguish (using Holl's terminology) main folds from adjacent folds in the juvenile pike. In the adult pike, we counted nine main folds, and were able to identify several type II folds and one type III fold (Holl, 1965; Fig. A.10B, red disks and black disk, respectively). In both the juvenile and the adult pike we were able to identify the fold likely to have developed first in the olfactory rosette (Fig. A.10, nasal fold 1; Holl, 1965). In the main text we refer to this fold as the central posterior nasal fold.

A.3. Further limitations of the models

Two further limitations of the models are:

1) The translucent part of the plastic model of the juvenile pike included the eye, but that of the adult pike (to make the model affordable) did not (Fig. 4).

2) The base of the pectoral fin was present in the plastic model of the juvenile pike (Fig. 4A, PF), but removed from the corresponding CFD model (Fig. A.4A, circle).

Given that the key elements of the pike's olfactory flow (Section 4.3) were present in both the dye visualisation experiments and the CFD simulations, neither difference is likely to have had a significant effect on olfactory flow.

A.4. Additional references

Barlow, J.B., Rae, W.H., Pope, A., 1999. Low-Speed Wind Tunnel Testing. 3rd ed. John Wiley & Sons, New York.

Garwood, R.J., Behnsen, J., Maclaine, J.S., Cox, J.P.L., 2020b. TIFF images from X-ray scan of nasal regions of *Esox lucius* (adult). Mendeley Data, v1. http://dx.doi.org/10.17632/zwk97m2y66.1.

Horne, A.J., Goldman, C.R., 1994. Limnology. 2nd ed. McGraw-Hill, New York.

James, R., Bennett, S., Neal, C., 2005. Water. The Open University, Milton Keynes.

Lim, T.T., 2000. Dye and smoke visualization. In: Smits, A.J., Lim, T.T. (Eds.), Flow Visualization. Imperial College Press, London, pp. 43-72.

Limaye, A., 2012. Drishti: a volume exploration and presentation tool. In: Stock, S.R. (Ed.), Proceedings SPIE 8506, Developments in X-ray Tomography VIII, 85060X.

Macan, T.T., 1974. Freshwater Ecology. 2nd ed. Longman, London.

A.5. Additional figures

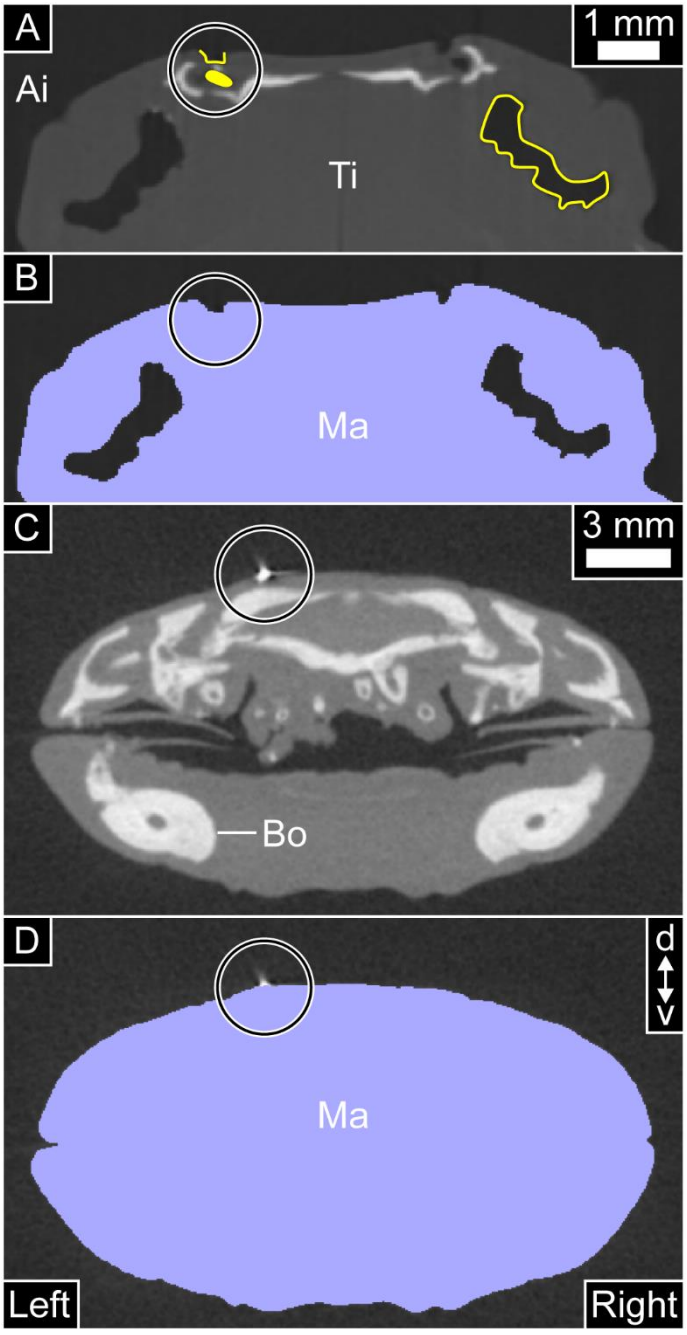

Fig. A.1. Image processing. (A) Dorsal part of TIFF image shown in Fig. 2A (from micro-CT scan of juvenile pike). Circle highlights lateral line pore (broken yellow line) and lateral line canal (filled yellow region). Continuous yellow line: perimeter of nasal chamber. (B) Same image as (A), with mask superimposed. (C) TIFF image from micro-CT scan of adult pike (transverse cross-section through head; location indicated by yellow marks in Fig. 1D). Circle highlights a feature caused possibly by a fragment of metal or glass. (D) Same image as (C),

with smoothed mask superimposed. Ai: Air; Bo: bone; d: dorsal; Ma: mask; Ti: tissue; v: ventral.

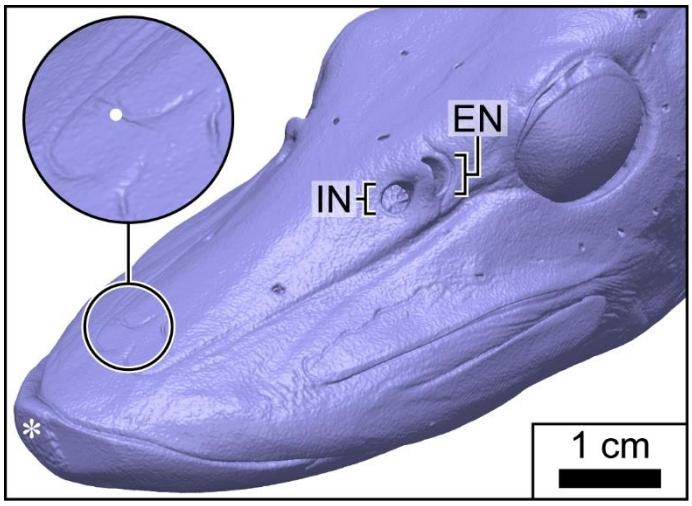

Fig. A.2. Surface model of adult pike after smoothing of head mask. Asterisk: location of micro-CT artifact on rostral tip. Inset: magnified rostral surface. White disk: location on specimen of possible fragment of metal or glass. EN: Excurrent nostril; IN: incurrent nostril.

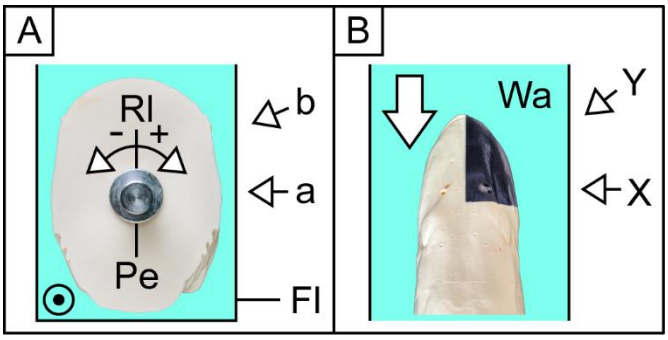

Fig. A.3. Camera positions and roll in the dye visualisation experiments. (A) Transverse cross-section of flume, showing posterior face of plastic model of adult pike. (B) Dorsal aspect of flume/plastic model of adult pike. Circular symbol (A) and large arrow (B): direction of free-stream flow (out of page for circular symbol). Arrows a, b, X, and Y: camera positions. Images not to scale. Fl: Flume; Pe: aluminium peg; Rl: roll angle; Wa: water.

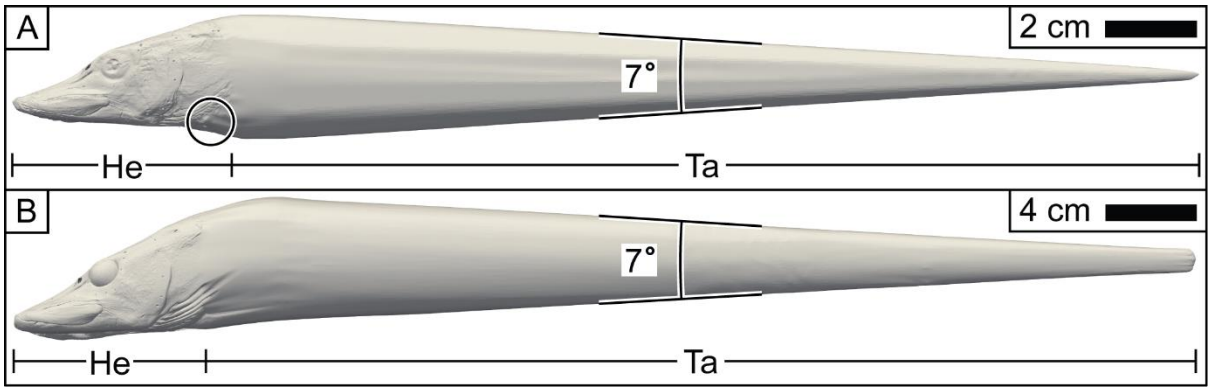

Fig. A.4. CFD models of (A) juvenile and (B) adult pike. Circle: removed pectoral fin. He: Head; Ta: tapered extension ('tail').

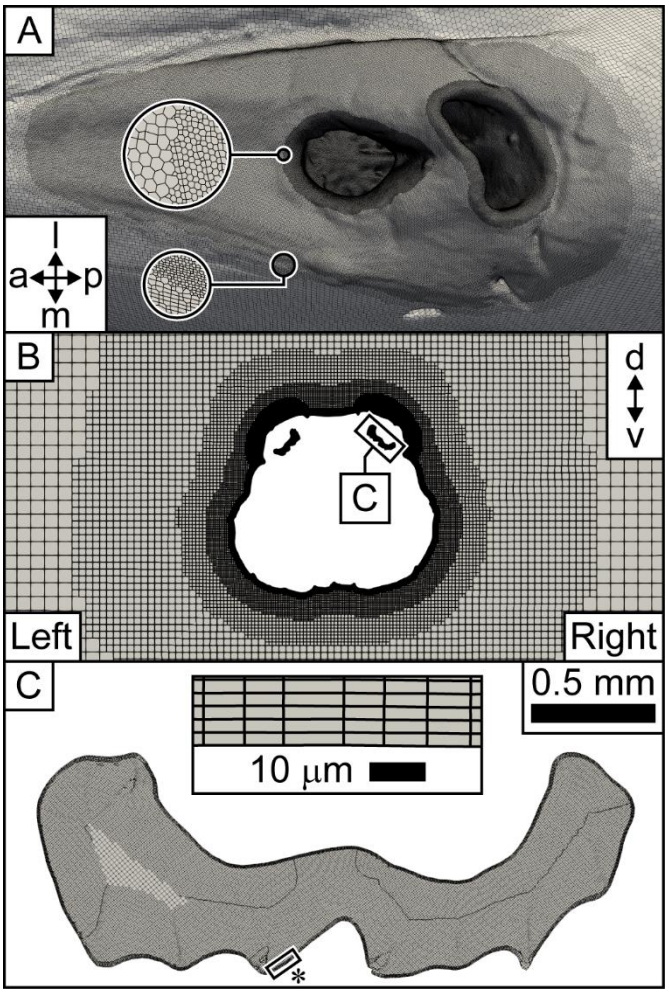

Fig. A.5. CFD mesh of juvenile pike. (A) Refinement of mesh on model surface, nasal region (superior view). Large circles: magnified border (small circles) at two stages of refinement, with refinement increasing bottom to top. (B) Transverse cross-section through mesh (same cross-section as in Fig. 2A). (C) Transverse cross-section through nasal passage. Inset in (C): mesh next to olfactory sensory surface (asterisked box, main image). Scale bars in (A) and (B) and labels in all images deliberately omitted to allow reader to see mesh. a: Anterior; d: dorsal; l: lateral; m: medial; p: posterior; v: ventral.

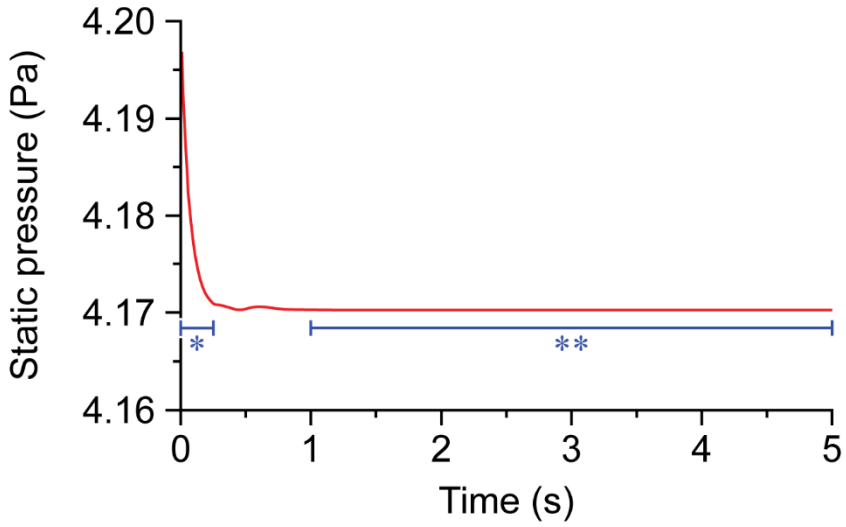

Fig. A.6. Variation in static pressure in transient CFD simulation of model of juvenile pike (yaw 0°). Static pressure monitored in the centre of the right incurrent nostril. Red line: variation in static pressure. Blue line/asterisk: time taken for nasal chamber to be flushed once (steady-state simulation). Blue line/double asterisk: period over which the variation in static pressure at the monitoring point is < 0.03 % of the average static pressure at that point over the same period.

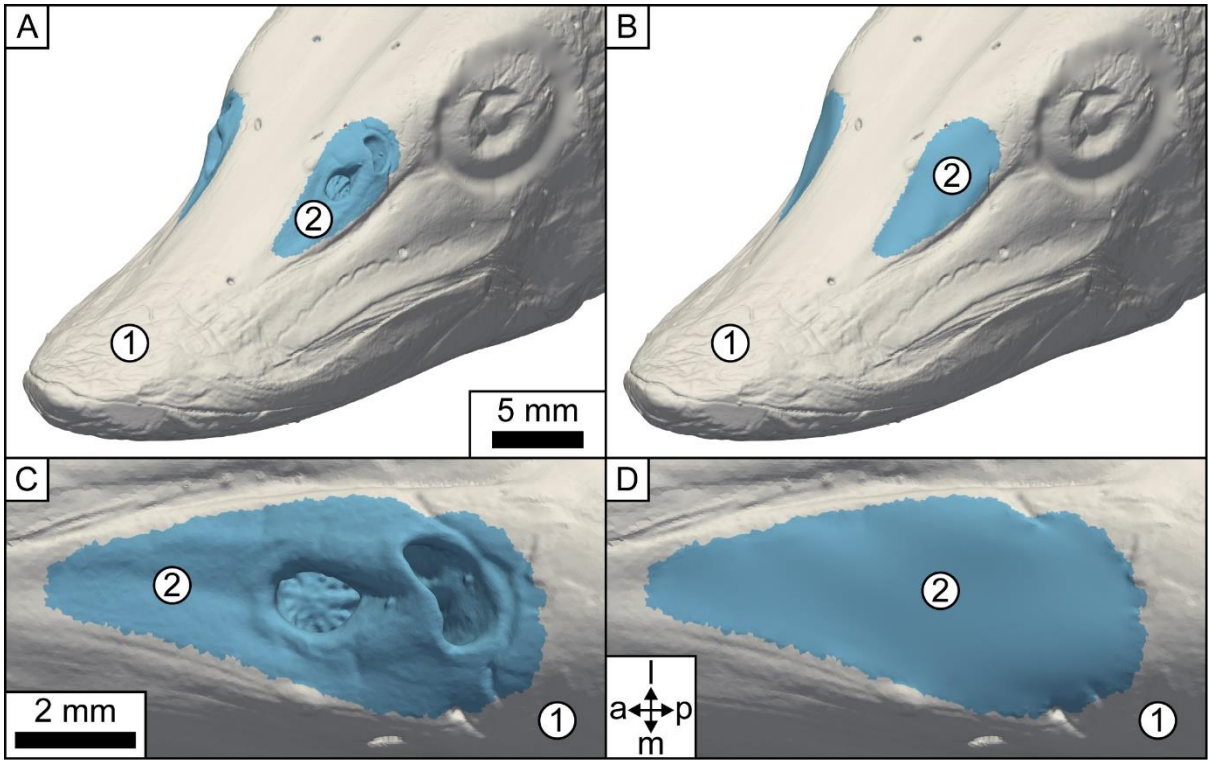

Fig. A.7. CFD models of juvenile pike used for drag measurements. (A) Head of 'wild type' model (nasal regions unaltered). (B) Head of 'mutant' model (nostrils and nasal chamber of each nasal region replaced by a continuous surface). (C) and (D): Nasal region of wild type and mutant model, respectively (superior view). Numbers indicate the regions for which drag forces were measured: 1) head (white; includes tail); 2) nasal region (blue). Scale bars in (A) and (C) also apply to (B) and (D), respectively. The CFD models of the adult pike were partitioned in the same way. a: Anterior; l: lateral; m: medial; p: posterior.

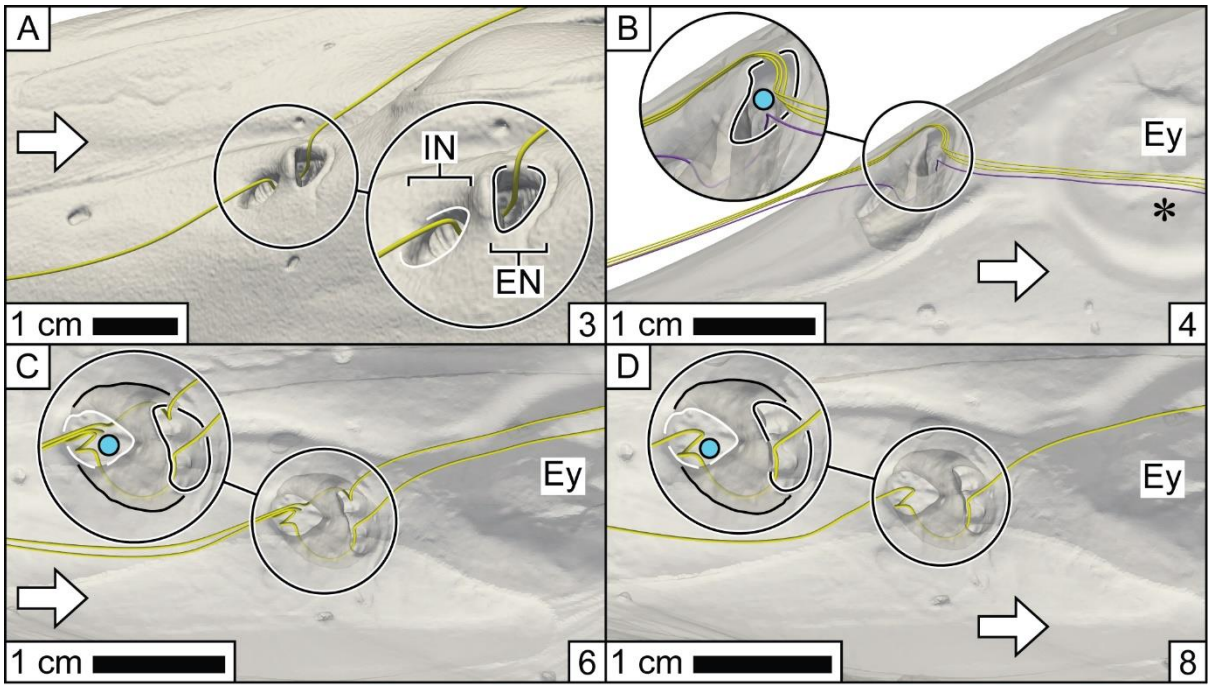

Fig. A.8. Correspondence of CFD-generated streamlines to olfactory flow in the plastic models of the pike. The plastic models are represented by surface models. Streamline(s) (tubes) correspond to dye behaviour in: (A) Video clip 3; (B) Video clip 4; (C) Video clip 6; and (D) Video clip 8 (video clip identified by number in box in each panel). (A) *Left* nasal region, adult pike; (B) – (D): nasal region, juvenile pike. (A): Dorsal aspect of model. (B): Lateral aspect. (C) and (D): Superior views. Insets: magnified nasal regions. Black lines in insets (C) and (D): extent of nasal chamber. Model in (B) – (D) at 50 % opacity, to match translucent right nasal region of plastic model. Scale bars refer to the size of the *plastic* models. Blue streamline in (B): flow passing through nasal chamber. Yellow streamlines in (B): flow participating in excurrent vortex. Arrow: direction of free-stream flow. Blue disk: vortex. Asterisk: (blue) streamline passing over eye. EN: Excurrent nostril (black on white lines); Ey: eye; IN: incurrent nostril (white lines).

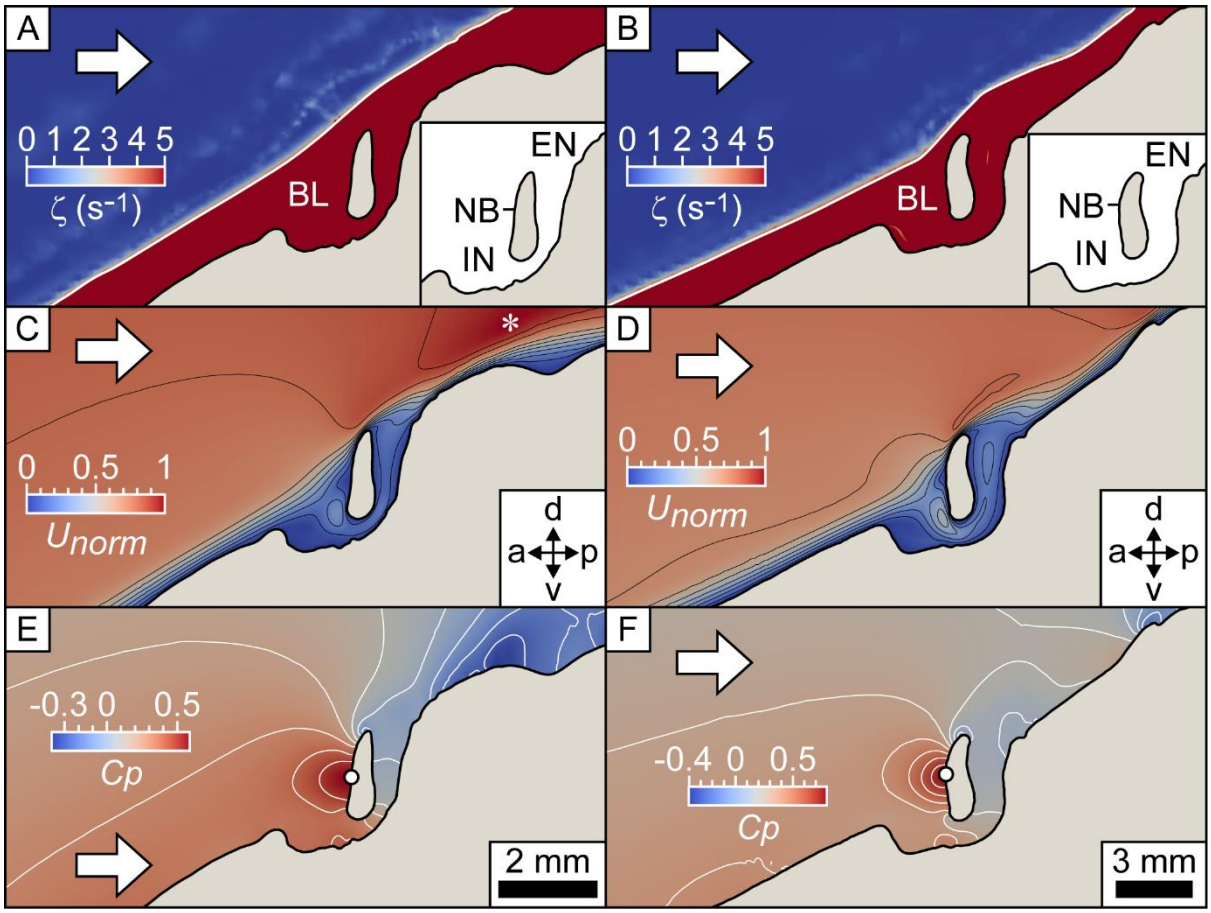

Fig. A.9. Sagittal slices through CFD mesh in nasal region of juvenile (A, C and E) and adult (B, D and F) pike. (A) and (B): Boundary layer, as defined by vorticity (ζ). White line: outer limit of boundary layer. Insets: key parts of nasal region. (C) and (D): Flow speed (*Unorm*), normalised to the maximum speed in each slice (asterisk in C). Black lines: contours of equal speed. (E) and (F): pressure coefficients (*Cp*). White disk: maximum *Cp*. White lines: isobars. Scale bar in (E) also applies to (A) and (C); scale bar in (F) also applies to (B) and (D). Arrow: direction of free-stream flow. a: Anterior; BL: boundary layer; d: dorsal; EN: excurrent nostril; IN: incurrent nostril; NB: nasal bridge; p: posterior; v: ventral.

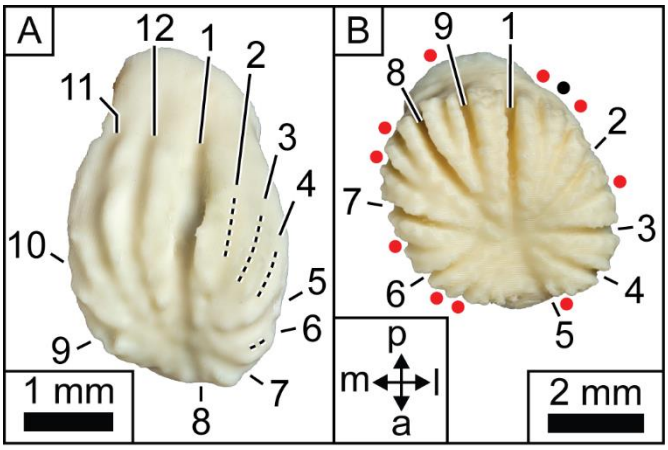

Fig. A.10. Plastic models of nasal volumes of pike. Ventral aspects. Nasal folds and sensory channels are represented by troughs and ridges, respectively. (A) Juvenile pike. Numbers: nasal folds. Dashed lines: locations (where not clear) of nasal folds. (B) Adult pike. Numbers: type I nasal folds (nomenclature according to Holl, 1965). Red disk: type II nasal fold. Black disk: type III nasal fold. Although the plastic models are larger than life, the scale bars refer to life-sized nasal volumes. a: Anterior; l: lateral; m: medial; p: posterior.